

Optimal estimation of snow and ice surface parameters from imaging spectroscopy measurements



Niklas Bohn ^{a,*}, Thomas H. Painter ^b, David R. Thompson ^c, Nimrod Carmon ^c, Jouni Susiluoto ^c, Michael J. Turmon ^c, Mark C. Helmlinger ^c, Robert O. Green ^c, Joseph M. Cook ^d, Luis Guanter ^e

^a GFZ German Research Centre for Geosciences, 14473 Potsdam, Germany

^b Joint Institute for Regional Earth System Science and Engineering, UCLA, Los Angeles, CA 90095-7228, USA

^c Jet Propulsion Laboratory, California Institute of Technology, Pasadena, CA 91109, USA

^d Department of Environmental Science - Environmental Microbiology and Circular Resource Flow, Aarhus Universitet, 4000 Roskilde, Denmark

^e Research Institute of Water and Environmental Engineering (IIAMA), Universitat Politècnica de València (UPV), 46022 Valencia, Spain

ARTICLE INFO

Keywords:

Imaging spectroscopy
Optimal estimation
Snow and ice
Light-absorbing particles in snow and ice
Greenland ice sheet
Atmospheric correction
EnMAP

ABSTRACT

Snow and ice melt processes are a key in Earth's energy-balance and hydrological cycle. Their quantification facilitates predictions of meltwater runoff as well as distribution and availability of fresh water. They control the balance of the Earth's ice sheets and are acutely sensitive to climate change. These processes decrease the surface reflectance with unique spectral patterns due to the accumulation of liquid water and light absorbing particles (LAP), that require imaging spectroscopy to map and measure. Here we present a new method to retrieve snow grain size, liquid water fraction, and LAP mass mixing ratio from airborne and spaceborne imaging spectroscopy acquisitions. This methodology is based on a simultaneous retrieval of atmospheric and surface parameters using optimal estimation (OE), a retrieval technique which leverages prior knowledge and measurement noise in an inversion that also produces uncertainty estimates. We exploit statistical relationships between surface reflectance spectra and snow and ice properties to estimate their most probable quantities given the reflectance. To test this new algorithm we conducted a sensitivity analysis based on simulated top-of-atmosphere radiance spectra using the upcoming EnMAP orbital imaging spectroscopy mission, demonstrating an accurate estimation performance of snow and ice surface properties. A validation experiment using in-situ measurements of glacier algae mass mixing ratio and surface reflectance from the Greenland Ice Sheet gave uncertainties of $\pm 16.4 \mu\text{g/g}_{\text{ice}}$ and less than 3%, respectively. Finally, we evaluated the retrieval capacity for all snow and ice properties with an AVIRIS-NG acquisition from the Greenland Ice Sheet demonstrating this approach's potential and suitability for upcoming orbital imaging spectroscopy missions.

1. Introduction

Snow and ice are the most variable surfaces on Earth with respect to their albedo, which ranges from 0.92 for fresh snow to less than 0.3 for snow contaminated with high loadings of light absorbing particles (LAP) (Flanner and Zender, 2006; Painter et al., 2012). The amount of absorbed solar radiation and the resulting melt processes are sensitive to the optical properties of snow and ice (Wiscombe and Warren, 1980), which are mainly determined by grain size as well as LAP type, mass mixing ratio, and size distribution (see Warren (1982); Aoki et al. (2003); Flanner and Zender (2006); Painter et al. (2001)). The accumulation of LAP at the snow surface, such as black carbon (BC), mineral dust, and

photosynthetic algae decreases the surface reflectance and leads to increased melting (Flanner et al., 2007). The resulting liquid water releases nutrients enclosed in-between the snow and ice grains so that algal growth is accelerated (Williamson et al., 2018). Furthermore, the grains tend to form clusters if liquid water is present and show similar optical properties as large grains (Dozier et al., 2009). Grain growth also occurs through sintering, and both liquid water and larger grains per se increase the absorptivity by BC as shown by Warren and Wiscombe (1980).

The detection and quantification of LAP accumulated in the upper snow and ice surface layer can provide a detailed basis for reconstructing physical and biological processes. In contrast to multispectral

* Corresponding author at: GFZ German Research Centre for Geosciences, Telegrafenberg, 14473 Potsdam, Germany.

E-mail address: nbohn@gfz-potsdam.de (N. Bohn).

sensors, imaging spectrometers can more accurately map the amounts of surface parameters based on the reflectance shape and magnitude (Painter et al., 2013). These instruments spectroscopically measure the solar radiation reflected by atmospheric and surface components in contiguous spectral channels and enable the identification and quantification of land, water, and atmosphere constituents using physically-based retrievals (Goetz et al., 1985; Schaepman et al., 2009).

The mapping of snow properties using imaging spectroscopy has been studied in great length for the past three decades. Techniques to estimate snow grain size first appeared in the early 80's and improved during the following years. Whereas Dozier et al. (1981), still lacking a suitable instrument, initially showed the potential of the near-infrared (NIR) to estimate grain size, Nolin and Dozier (1993) introduced a method based on the snow reflectance at 1030 nm using data from the National Space and Aeronautics Administration (NASA)'s Airborne Visible Infrared Imaging Spectrometer (AVIRIS). They inverted a model built upon the nonlinear relationship between modeled directional reflectance and snow grain size. This approach was subsequently extended to the complete 1030 nm ice absorption feature by relating the absorption band area to snow grain size (Nolin and Dozier, 2000), and improved by taking into account snow subpixel cover (Painter et al., 2003). Painter et al. (2013) reduced biases due to liquid water and water vapor absorption by introducing a spectral fitting approach between a modeled snow spectrum and surface reflectance observed by the instrument. A detailed analysis of spatial and temporal variability of snow properties is presented in Seidel et al. (2016), and the retrieval techniques have been further improved by combining imaging spectroscopy with scanning lidar to develop the Airborne Snow Observatory (ASO), providing a comprehensive suite of snow retrieval algorithms (Painter et al., 2016).

While these approaches consistently use atmospherically corrected spectra to retrieve snow surface parameters, several studies have been introduced to map snow and ice properties with simultaneously accounting for the effect of the atmosphere based on data from the Moderate Resolution Imaging Spectroradiometer (MODIS). A prominent example is the snow grain size and pollution amount (SGSP) algorithm, which has been applied to retrieve snow grain size and soot concentration (Zege et al., 2008, 2011; Carlsen et al., 2017). But also, a retrieval of snow subpixel cover from MODIS top-of-atmosphere (TOA) radiance has been presented (Sirguey et al., 2009).

The effects of liquid-water coatings around snow grains have initially been incorporated into reflectance models for melting snow by Green et al. (2002). To facilitate a discrimination between wet and dry snow and to provide a basis for meltwater runoff predictions, Green et al. (2006) also developed a method to simultaneously retrieve the optical path lengths of the three phases of water over melting snow from AVIRIS measurements. Their approach was also transferred to synthetic spaceborne EnMAP data (Bohn et al., 2020).

Many previous studies have investigated the influence of inorganic LAP, such as BC and mineral dust, and their size distributions on the snow and ice surface reflectance and incorporated their effects into radiative transfer models (RTM) (see Clarke and Noone (1985); Flanner et al. (2007); Brandt et al. (2011); Hadley and Kirchstetter (2012); Skiles and Painter (2018)). Absorption of radiation by biological LAP, mainly snow algae, have also been shown to increase rates of melt on the Greenland Ice Sheet (Yallop et al., 2012) and in seasonal snow at middle latitudes. Their retrieval from imaging spectroscopy has also been demonstrated.

The first approach was shown by Painter et al. (2001), who developed a method to detect and quantify concentrations of blooms of snow algae based on a model for the integral of the continuum-scaled 680 nm chlorophyll absorption feature. They used field measurements of the spectral hemispheric conical reflectance factor (HCRF) and snow algal concentration to build the model and applied it to AVIRIS data. However, they did not perform a ground truth validation of the retrieval results. Takeuchi et al. (2006) found a relationship between the

reflectance ratio of the red to the green visible (VIS) wavelengths and snow algal biomass. They used multispectral satellite data to estimate distribution and abundance of snow algae. Recently, Gray et al. (2020) presented a quantification of green snow algae biomass using the chlorophyll-a absorption at 680 nm based on multispectral Sentinel-2 data.

Both Takeuchi et al. (2006) and Gray et al. (2020) validated their estimated spectral relationships such as band ratio and absorption feature depth with ground reflectance measurements, but they likewise did not conduct a direct ground truth validation of the estimated algal biomass. Both studies mention the limitations of multispectral satellite sensors to detect algal blooms, which confirms the need for high-resolution orbital imaging spectroscopy missions to quantify LAP in snow and ice. In order to estimate the effects of algae on snowmelt, Cook et al. (2017b) coupled a biooptical model and an RTM to predict the spectral reflectance of snow contaminated with algal LAP. Based on this model, it was demonstrated that glacier algae indeed accelerate snow melting on the Greenland Ice Sheet by increasing the radiative forcing (Cook et al., 2020).

Especially in view of upcoming orbital missions, imaging spectroscopy of snow and ice faces new possibilities. For instance, the Greenland Ice Sheet is the largest single contributor to global sea level rise (Bamber et al., 2018), but is remote and difficult to access. Besides already existing orbital acquisitions from multispectral sensors, spaceborne imaging spectrometers will significantly increase the amount of data available on a regular basis. They can therefore further improve our understanding of melt processes on snow and ice surfaces, which is essential to evaluate the associated impacts on climate change (Stibal et al., 2017).

Several orbital imaging spectroscopy missions were recently or soon will be launched. The German Aerospace Center's (DLR) Earth Sensing Imaging Spectrometer (DESI) (Mueller et al., 2016) and the Italian Hyperspectral Precursor of the Application Mission (PRISMA) (Loizzo et al., 2018) are in operation since June 2018 and March 2019, respectively. The German Environmental Mapping and Analysis Program (EnMAP) (Guanter et al., 2015) and NASA's Earth Surface Mineral Dust Source Investigation (EMIT) (Green et al., 2018) are scheduled for launch in early 2022. Additionally, NASA's Surface Biology and Geology (SBG) investigation (National Academies, 2018) is in formulation, and the Copernicus Hyperspectral Imaging Mission (CHIME) (Rast et al., 2019) led by ESA is in the planning phase and considered for operation starting around 2027.

This work presents a new method to retrieve snow and ice parameters for semi-homogeneous surfaces from imaging spectroscopy data. We use a framework of a simultaneous retrieval of atmospheric and surface parameters following the approach presented in Thompson et al. (2018). The method is based on an optimal estimation procedure incorporating prior knowledge and measurement noise as well as model uncertainties. While Thompson et al. (2018) use statistics calculated from a comprehensive collection of measured reflectance spectra as prior knowledge of the surface state, we extend the prior distributions by assigning additional snow and ice parameters such as grain size or LAP mass mixing ratios to each spectrum. We calculate the reflectance statistics based on many runs of the physical snow RTM BioSNICAR-GO (Cook et al., 2020).

We evaluate the performance of the algorithm through a sensitivity analysis, present retrieval uncertainties, and discuss the potential for future orbital imaging spectroscopy missions. Additionally, we validate the approach of the extended surface model by comparing our results with field observations of surface reflectance and algae mass mixing ratios from the Greenland Ice Sheet. Finally, we use data from NASA's Next Generation AVIRIS (AVIRIS-NG) to demonstrate the ability of the algorithm to realistically map snow and ice surface parameters.

2. Methods

2.1. Optimal estimation

We determine statistical correlations between surface parameters and surface reflectance, and then use these to inform a simultaneous Bayesian inversion of surface and atmospheric parameters. We apply an extended version of the method introduced by Thompson et al. (2018). The approach is based on the probabilistic formalism of Rodgers (2000), known as Optimal Estimation (OE). In-depth details of the mathematical expressions presented in this section can be found in both mentioned references. Following standard conventions, we use uppercase boldface to indicate matrices and a lowercase boldface notation for vectors and vector-valued functions.

We use a set of measured TOA radiances, combined in the measurement vector $\mathbf{y} = [y_1, \dots, y_m]^T$, to estimate the state vector $\mathbf{x} = [x_1, \dots, x_n]^T$ by inverting a well-parameterized forward model $\mathbf{f}(\mathbf{x})$. It models TOA radiance for a given combined atmosphere and surface state using an atmospheric RTM. More details on \mathbf{f} are provided in Section 2.2. In general form, \mathbf{f} can be written as a vector-valued function depending on the state vector \mathbf{x} and yielding the measurement vector \mathbf{y} :

$$\mathbf{y} = \mathbf{f}(\mathbf{x}) + \boldsymbol{\varepsilon}, \quad (1)$$

where \mathbf{x} is composed of an atmospheric state vector \mathbf{x}_{ATM} and a surface state vector \mathbf{x}_{SURF} . $\boldsymbol{\varepsilon}$ is a random error vector representing measurement noise and instrument calibration errors as well as a priori uncertainties in the state vector variables and errors due to unknown forward model parameters.

We invert the forward model by iteratively minimizing the scalar-valued cost function $\chi^2(\mathbf{x})$, which is commonly used for OE procedures. By linearizing the forward model and assuming Gaussian error statistics, this is the part of the negative log posterior that is sensitive to changes in the state vector \mathbf{x} :

$$\chi^2(\mathbf{x}) = \frac{1}{2}(\mathbf{x} - \mathbf{x}_a)^T \mathbf{S}_a^{-1} (\mathbf{x} - \mathbf{x}_a) + \frac{1}{2}(\mathbf{y} - \mathbf{f}(\mathbf{x}))^T \mathbf{S}_e^{-1} (\mathbf{y} - \mathbf{f}(\mathbf{x})), \quad (2)$$

where \mathbf{x}_a is the a priori state vector with the associated error covariance matrix \mathbf{S}_a ; and \mathbf{S}_e is the measurement error covariance matrix. The cost function penalizes differences between the modeled spectrum $\mathbf{f}(\mathbf{x})$ and the measured spectrum \mathbf{y} , and between the estimated state and the prior, by taking into account their uncertainties. At each iteration step, the state vector is changed to reduce the value of the cost function until a local minimum is reached. Finally, the state with the highest probability given the measurement and the a priori state is reported. It must be noted that in some cases of a nonlinear problem the iteration may approach a local minimum so that the reported solution state and the associated posterior predictive uncertainties may not be the required solution. Existing literature only marginally attends to the question of correct convergence (Cressie, 2018). However, we assume our approach to be stable as the initial guess tends to be within $\pm 10\%$ of the full probabilistic solution (see Section 2.3).

\mathbf{S}_e decomposes into a matrix \mathbf{S}_y comprising uncertainties due to physical instrument noise, and a matrix \mathbf{S}_b that accounts for errors introduced by unknown forward model parameters.

\mathbf{S}_y is calculated by:

$$\mathbf{S}_{j,k}^y = c_{j,k} \sigma_{y,j} \sigma_{y,k}, \quad (3)$$

where $\sigma_{y,j}$ and $\sigma_{y,k}$ are the standard deviations of the measurement errors for the j -th and k -th band of the imaging spectrometer; and $c_{j,k}$ is the error correlation coefficient between the j -th and k -th band. For standard imaging spectrometers, we assume $c_{j,k} = 0$ when $j \neq k$. Consequentially, \mathbf{S}_y is diagonal having the following elements, which are the noise-equivalent changes in radiance for each instrument channel:

$$(\delta_{j,j}^y)^2 = \left(\frac{L_j}{SNR_j} \right)^2 + \Delta_j^2, \quad (4)$$

where L_j is the measured radiance in band j ; SNR_j is the radiance-dependent signal-to-noise ratio (y/σ_y) of band j ; and Δ_j is the calibration uncertainty of band j .

\mathbf{S}_b holds covariances of forward model parameters which are uncertain and might affect the measurement, but which are not retrieved as part of the state vector. Following Thompson et al. (2018), they can originate from the surface, the instrument, or the atmosphere. They can include sky view effects, intrinsic errors in water vapor absorption coefficients, systematic calibration and radiative transfer uncertainty as well as non-systematic radiometric uncertainty. We assume them to be independent error sources and add their contributions to \mathbf{S}_y :

$$\mathbf{S}_e = \mathbf{S}_y + \mathbf{K}_b \mathbf{S}_b \mathbf{K}_b^T, \quad (5)$$

where \mathbf{K}_b is the Jacobian of the forward model comprised of partial derivatives with respect to the not retrieved model unknowns:

$$\mathbf{K}_{i,j}^b = \frac{\partial y_i}{\partial b_j}. \quad (6)$$

We adopt uncertainties of sky view effects and water vapor absorption intensity from Thompson et al. (2018) being 10% and 1%, respectively. The former is assumed to be the maximum error in the fraction of the hemispherical sky illumination that is visible from the surface, the latter is based on validation of the HITRAN database (Rothman et al., 2009). Although the sky view is likely nearly 1.0 over the Greenland Ice Sheet, we decided to choose a conservative value for \mathbf{S}_b in order to capture the variability of the sky view factor in the way it is used by RTMs. Since our sensitivity analysis is based on simulated data, we do not include any systematic and non-systematic errors.

The OE approach enables the interpretation of the retrieval uncertainty by providing several metrics of error analysis. Besides the optimized and converged state vector, the method calculates the posterior predictive error distribution by means of the retrieval error covariance matrix $\widehat{\mathbf{S}}$:

$$\widehat{\mathbf{S}} = (\mathbf{K}^T \mathbf{S}_e^{-1} \mathbf{K} + \mathbf{S}_a^{-1})^{-1}, \quad (7)$$

where \mathbf{K} is the Jacobian of the forward model comprised of partial derivatives with respect to the state vector \mathbf{x} :

$$\mathbf{K}_{i,j} = \frac{\partial y_i}{\partial x_j}. \quad (8)$$

A similar quantity to \mathbf{K} is the gain matrix \mathbf{G} , which indicates the sensitivity of the solution state vector to the measurement:

$$\mathbf{G} = (\mathbf{K}^T \mathbf{S}_e^{-1} \mathbf{K} + \mathbf{S}_a^{-1})^{-1} \mathbf{K}^T \mathbf{S}_e^{-1}. \quad (9)$$

\mathbf{G} is used to construct the averaging kernel matrix \mathbf{A} :

$$\mathbf{A} = \mathbf{G} \mathbf{K}. \quad (10)$$

It contains several measures of the retrieval characteristics at the same time. On the diagonal, it provides the Degrees of Freedom (DOF) for each state vector parameter and consequently, the trace of \mathbf{A} represents the total DOF of the retrieval. Rows of \mathbf{A} are the averaging kernels and give the sensitivity of a particular parameter of the solution state to different elements of the true state. The columns show the impulse response of the solution state to a small change in a particular parameter of the true state.

2.2. Forward model

Our forward model \mathbf{f} is a function of the state vector \mathbf{x} , which contains the free parameters that are optimized throughout the iteration

procedure. All components of \mathbf{x} are changed with each iteration until the most probable solution state vector $\hat{\mathbf{x}}$ is found. \mathbf{x} is split in an atmospheric part $\mathbf{x}_{\text{ATM}} = [x_{\text{H2O}}, x_{\text{AOT}}]^T$ including the columnar water vapor in g cm^{-2} and the dimensionless Aerosol Optical Thickness (AOT) at 550 nm, and a surface part $\mathbf{x}_{\text{SURF}} = [x_{\lambda 1}, \dots, x_{\lambda m}, x_{\text{SURF1}}, \dots, x_{\text{SURFn}}]^T$, which includes the also dimensionless surface reflectance for each of m instrument channels with center wavelengths $[\lambda_1, \dots, \lambda_m]$ and n additional surface parameters. Details on the reflectance quantity we are referring to are provided in Section 2.2.1. We only retrieve water vapor and AOT for the atmospheric part since they belong to the few temporally-variable parameters of the atmosphere, which mainly determine the shape of the TOA radiance spectrum and can usefully be estimated with imaging spectroscopy (Thompson et al., 2018). The additional surface parameters retrieved in our study are the snow grain radius in μm , the liquid water fraction in percent as well as mass mixing ratios of snow algae, glacier algae, BC, and mineral dust, all in units of $\mu\text{g/g}_{\text{snow/ice}}$. Although the additional surface variables are part of the state vector, they do not serve as an input to our forward model. We call this a ‘lazy’ prior-driven inversion since the optimization of those parameters is entirely based on their prior mean and covariance, whose derivation is presented in Section 2.2.3.

2.2.1. Atmosphere radiative transfer model

For the atmosphere model we use the same setup as described in Bohn et al. (2020), which relies on radiative transfer simulations by the MODTRAN code (Berk et al., 1989). It enables the calculation of atmospheric radiation components for the ultraviolet (UV), VIS, NIR, shortwave-infrared (SWIR), and thermal infrared (TIR) spectrum covering a wavelength range of 0.2– $10^4 \mu\text{m}$ in a one-dimensional space. To match the optical spectral range, we simulated gaseous transmittance, radiance, and fluxes spanning wavelengths from 400 nm to 2500 nm. We selected the MODTRAN band model mode choosing a spectral sampling interval (SSI) of 1.0 cm^{-1} . To calculate gaseous transmittance, MODTRAN uses absorption lines taken from the HITRAN database (Rothman et al., 2009), and performs multiple scattering simulations based on the DISORT N-stream program (Stamnes et al., 1988).

We follow the approach of Chandrasekhar (1960) and model the TOA radiance L_{TOA} at a specific wavelength by a simplified solution of the radiative transfer equation:

$$L_{\text{TOA}} = L_0 + \frac{1}{\pi} \frac{\rho_s (E_{\text{dir}} \mu_{\text{sun}} + E_{\text{dif}}) T_{\uparrow}}{1 - S \rho_s}, \quad (11)$$

where L_0 is the atmospheric path radiance; E_{dir} and E_{dif} are the direct and diffuse solar irradiance arriving at the surface; μ_{sun} is the cosine of the solar zenith angle; T_{\uparrow} is the total upward atmospheric transmittance; and S is the spherical albedo at bottom of atmosphere (BOA). The parameter ρ_s expresses the dimensionless surface reflectance, whose quantity is determined by the RTM selected for calculating the prior statistics.

In case of a Lambertian, horizontal, infinite, and isotropic surface, the incident solar radiation is equally reflected in all directions. However, like all natural surfaces, snow and ice reflectance shows a certain degree of spectrally-variant anisotropy (Painter and Dozier, 2004a; Schaepman-Strub et al., 2006). This means that the scattering of light follows an angular distribution in terms of directional reflectance or the hemispherical directional reflectance factor (HDRF). It is controlled by snow texture, grain morphology, solar zenith angle, liquid water content, LAP concentration, and surface roughness (Painter and Dozier, 2004b). Measurements taken by an airborne or spaceborne imaging spectrometer sample from the HDRF, with varying SZA across the seasons and a range of VZA depending on the instrument angle and the local topography (Schaepman-Strub et al., 2006). However, as we assume clear sky and a plane-parallel atmosphere as well as a Lambertian, infinite, horizontal, and isotropic surface, ρ_s is representing the spectral albedo in our modeling. It is defined as the integral of all HDRF over the

Table 1

Gridding of LUT parameters for MODTRAN radiative transfer simulations according to Guanter et al. (2009).

	1	2	3	4	5	6	7
VZA (°)	0	10	20	30	40	–	–
SZA (°)	0	10	20	35	50	70	–
RAA (°)	0	25	50	85	120	155	180
HSF (km)	0	0.7	2.5	8	–	–	–
AOT	0.05	0.12	0.2	0.3	0.4	0.8	–
CWV (g cm^{-2})	0	1	1.5	2	2.7	3.5	5

Varied parameters include VZA, SZA, RAA, surface elevation (HSF), AOT, and columnar water vapor (CWV).

full hemisphere (Dozier et al., 2009):

$$\alpha_{\lambda}(\theta_0, r) = \int_0^{2\pi} \int_0^{\frac{\pi}{2}} \text{HDRF}_{\lambda}(\theta_0, \theta_v, \phi, r) \cos \theta_v \sin \theta_v d\theta_v d\phi, \quad (12)$$

where θ_0 , θ_v , and ϕ represent solar zenith angle (SZA), view zenith angle (VZA), and relative azimuth angle (RAA), respectively; and r is the snow grain radius. An appropriate measure to quantitatively express the difference between spectral albedo and HDRF is given by the spectral anisotropy factor c . It is defined as the ratio of spectral albedo to HDRF (Painter et al., 2013):

$$c_{\lambda}(\theta_0, \theta_v, \phi, r) = \frac{\alpha_{\lambda}(\theta_0, r)}{\text{HDRF}_{\lambda}(\theta_0, \theta_v, \phi, r)}. \quad (13)$$

Substituting HDRF for spectral albedo is accurate for near-nadir acquisitions over a horizontal surface since snow property retrievals are only slightly affected by directional reflectance under these conditions (Painter and Dozier, 2004a; Dumont et al., 2010). As we use EnMAP nadir simulations and subsets from an AVIRIS-NG acquisition covering almost flat surfaces on the Greenland Ice Sheet, simulations of spectral albedo in place of HDRF are sufficient to demonstrate the principles of our inversion. Furthermore, the HDRF of snow is less anisotropic for wavelengths below 1000 nm (Painter and Dozier, 2004b), so that the retrieval of LAP concentration, being primarily absorptive in the VIS, will be less affected by varying solar and observation geometries. Nevertheless, a more detailed treatment with a broad range of LAP inclusions in a directional modeling will come in subsequent work. A detailed discussion of our choice is given in Section 4.1.4.

The free parameters of the atmospheric state are implicitly included since all components of the right side of Eq. (11) except ρ_s are functions of \mathbf{x}_{ATM} . The free parameters of the surface appearing in our forward model, $[x_{\lambda 1}, \dots, x_{\lambda m}]$, are expressed by ρ_s for each particular wavelength.

We apply the algebraic conversions presented in Guanter et al. (2009) to obtain L_0 , E_{dir} , E_{dif} , T_{\uparrow} , and S from the original MODTRAN output. We ran the RTM for various atmospheric states and observation geometries, which we assume to comprise most of the possible acquisition conditions of the instruments used in this study, and built a multidimensional Look-Up-Table (LUT) containing all atmospheric components (Table 1) (see Bohn et al. (2020)).

The atmospheric priors are constructed as an unconstrained diagonal covariance matrix. For simplicity, we assume no intercorrelation.

2.2.2. Snow and ice radiative transfer model

RTMs for snow and ice generally use the effective snow grain radius for parameterizing the geometry of the surface particles. It is the area-weighted mean radius of the snow grains within a specific surface area (Warren, 1982). However, in order to obtain the effective grain radius, several different approaches exist to model the shape of snow and ice particles. One of the most commonly used methods is to model non-spherical snow particles as a collection of spheres using Lorenz-Mie calculations (Grenfell and Warren, 1999). This approach is based on the assumption that the effective snow grain radius is much larger than the incident radiation wavelengths. Thereby, the scattering of

electromagnetic radiation from a sphere of a particular medium is approximated by computing the extinction efficiency, the single scattering albedo, and the scattering asymmetry factor (Wiscombe, 1980). Applying the collected-spheres approach, extinction efficiency and single scattering albedo of snow are accurately expressed (Warren, 2019). However, the scattering asymmetry factor tends to be overestimated using this method so that its effect needs to be corrected by slightly reducing the effective snow grain radius in model simulations (Dang et al., 2016).

A different technique was introduced by Aoki et al. (2007), who come up with three types of dimensions for defining snow grain size. They consider length, width, and thickness of the ice crystals. Kokhnovsky and Zege (2004) likewise pointed to the limitations of the collected-spheres approach due to the irregular shaped ice crystals. They present a calculation of snow optical properties based on geometric optics (GO) equations. Hereinafter, this method has been refined by combining GO with a stereological approach that considers snow as a two-phase mixture of ice particles and air (Malinka, 2014). Ultimately, Libois et al. (2013) introduced a grain shape model based on only two parameters: the absorption enhancement parameter and the geometric asymmetry factor. They assume GO and a weak snow absorption while illustrating the limitations of the collected-spheres approach.

It is not straightforward though to reproduce these parameterization approaches empirically since measuring the snow effective grain size in the field is challenging (Cook et al., 2017a). The grain radius can be estimated accurately using contact spectroscopy (Painter et al., 2007), whereas the observed quantity from hand lenses is different and cannot be equalized with the effective radius as it does not describe the full path length of the ice absorption (Cook et al., 2017a). Other instruments to measure snow grain radius in the field comprise laser diodes in combination with an integrating sphere or a high-resolution penetrometer (Gallet et al., 2009; Arnaud et al., 2011; Proksch et al., 2015). Although some studies tried to develop a reproducible relationship between the observed and the effective grain radius (see Painter et al. (2007)), a direct validation of the RTM assumptions is still difficult.

We use the snow and ice RTM BioSNICAR-GO to calculate the prior reflectance statistics and the input reflectance spectra for our sensitivity analysis (see Sections 2.2.3 and 3.1). The model is available as Python package and was developed by Cook et al. (2020). They coupled a bio-optical model with the two-stream multilayer SNOW, ICe, and Aerosol Radiation model SNICAR (Flanner et al., 2007). The latter is built on the theory of Wiscombe and Warren (1980) and the two-stream approximations of Toon et al. (1989), which enable the modeling of heterogeneous snow properties in multiple vertical layers. Additionally, the effects of the underlying surface reflectance can be incorporated into the model.

BioSNICAR-GO provides a coupling between a bio-optical model, Mie and GO modeling, and a two-stream RTM. It offers the possibility to model optical properties either based on Lorenz-Mie calculations for snow and small LAP such as BC, mineral dust, and snow algae, or based on the GO approach for large ice crystals and glacier algae. In GO mode, the ice optical properties are calculated using a parameterization of the geometric optics approach as described by van Diedenhoven et al. (2014). Especially the possibility to use GO for modeling ice crystals shaped as arbitrarily large hexagonal plates and columns guided us in selecting BioSNICAR-GO.

For incorporating the effect of liquid water, we coupled BioSNICAR-GO with one of the spectral snow-reflectance models developed for melting snow by Green et al. (2002). It uses two-layer coated sphere Lorenz-Mie calculations to increase the snow grain radius by a particular liquid water fraction, and is based on the partially different optical properties of liquid water and ice. While over much of the solar spectrum, they are similar, the differences are most acute near the local absorption features, such as the 980 nm water and the 1030 nm ice features that Green et al. (2006) exploit for liquid water and grain size retrievals in a subsequent study. Green et al. (2002) also show that the

Table 2

Values and step sizes used for calculating the prior surface statistics.

Parameter	min, ..., max	Step size
Snow Grain Radius [μm]	50, ..., 1500	10
Ice Crystal Side Length and Diameter [μm]	1000, ..., 30,000	1000
Liquid Water Fraction [%]	0, ..., 25	5
Snow Algae (<i>C. nivalis</i>) [$\mu\text{g/g}_{\text{snow}}$]	0, ..., 400	10
Glacier Algae (<i>M. berggrenii</i>) [$\mu\text{g/g}_{\text{ice}}$]	0, ..., 400	20
Glacier Algae (<i>A. nordenskioldii</i>) [$\mu\text{g/g}_{\text{ice}}$]	0, ..., 400	20
BC [$\mu\text{g/g}_{\text{snow/ice}}$]	0, ..., 1	0.1
Mineral Dust [$\mu\text{g/g}_{\text{snow/ice}}$]	0, ..., 400	40

coated spheres approach is more accurate than accounting for liquid water as separate spheres mixed with ice crystals. However, the scattering properties of a mixture of water and ice are not rigorously treated by radiative transfer models yet (Dozier et al., 2009). Although confirming the partial validity of the coated spheres approach, Gallet et al. (2014) conclude that both optical models presented in Green et al. (2002) are not ideal to reproduce the water-ice distribution in wet snow. Water in snow causes grains to cluster, so that they behave as larger grains, affecting snow albedo through much of the NIR and SWIR (Colbeck, 1979). Alternatively, one might model the effect of liquid water in snow by simply increasing the grain radius, but as the transparency of ice has a significant impact on the penetration depths of different wavelengths, this approach might lead to erroneous retrieval results (Dozier et al., 2009).

Based upon the optical properties obtained from Mie or GO modeling, the spectral albedo, subsurface light field, and the energy absorbed per vertical layer can be simulated using the two-stream RTM. Here, we define several input parameters including number and thickness of vertical layers, snow density, grain size, liquid water fraction as well as types and mass mixing ratios of LAP (for details, see Section 2.2.3). However, the physical manifestation of snow spectral albedo is arrived at from complex intersection of different metrics. They include the estimation of effective grain size and shape, LAP spectral optical properties and size distribution, their location in or out of the grains or matrix as well as the presence and geometry of liquid water. Present measurement capabilities are inadequate to constrain all of the above physical drivers. Hence, we balance complexity with assumptions to enable solution of the inverse problem.

2.2.3. Prior surface statistics

We use an extended version of the approach presented in Thompson et al. (2018) to model the surface. Besides the spectral albedo ρ_s (see Eq. (11)), x_{SURF} also includes additional surface parameters, which are not needed by our forward model but optimized throughout the inversion. Consequentially, direction and gradient of $[x_{\text{SURF}1}, \dots, x_{\text{SURFn}}]$ during the iteration are exclusively guided by the prior knowledge. The surface prior is a multivariate Gaussian with mean \mathbf{x}_s and covariance \mathbf{S}_s . We treat the additional surface parameters as unobserved instrument channels that are related to observed reflectance channels by a joint mean and covariance. \mathbf{S}_s is not diagonal as we expect correlations across channels to occur ensuring physical plausibility and numerical stability.

Whereas Thompson et al. (2018) used a collection of measured reflectance spectra as prior surface statistics, we simulated snow and ice spectra for a range of grain sizes and crystal dimensions using BioSNICAR-GO (see Section 2.2.2). We perturbed the simulations by varying liquid water fractions and different types and mass mixing ratios of LAP. Table 2 shows minimum and maximum values as well as step sizes chosen for calculating the prior statistics.

We selected hydrophobic uncoated spheres of BC and optical properties of Greenland dust, which have similar complex refractive indices as the global average of Saharan dust in the SNICAR library (Flanner et al., 2007, 2009). The choice of range and step size was guided by observed and retrieved values presented in various studies. We defined a typical snow grain radius range of 50 – 1000 μm with extreme values of

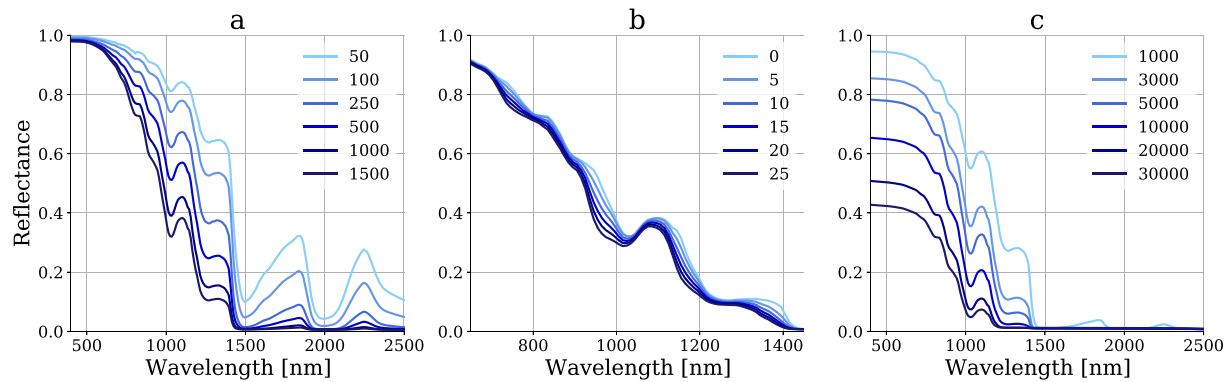


Fig. 1. Snow and glacier ice surface reflectance modeled using BioSNICAR-GO for a) different snow grain radii [μm]; b) different liquid water fractions [%] for a grain radius of $1500 \mu\text{m}$ (for clarity, only the spectral interval from 650 to 1450 nm is shown); c) different side lengths and diameters of glacier ice grains [μm].

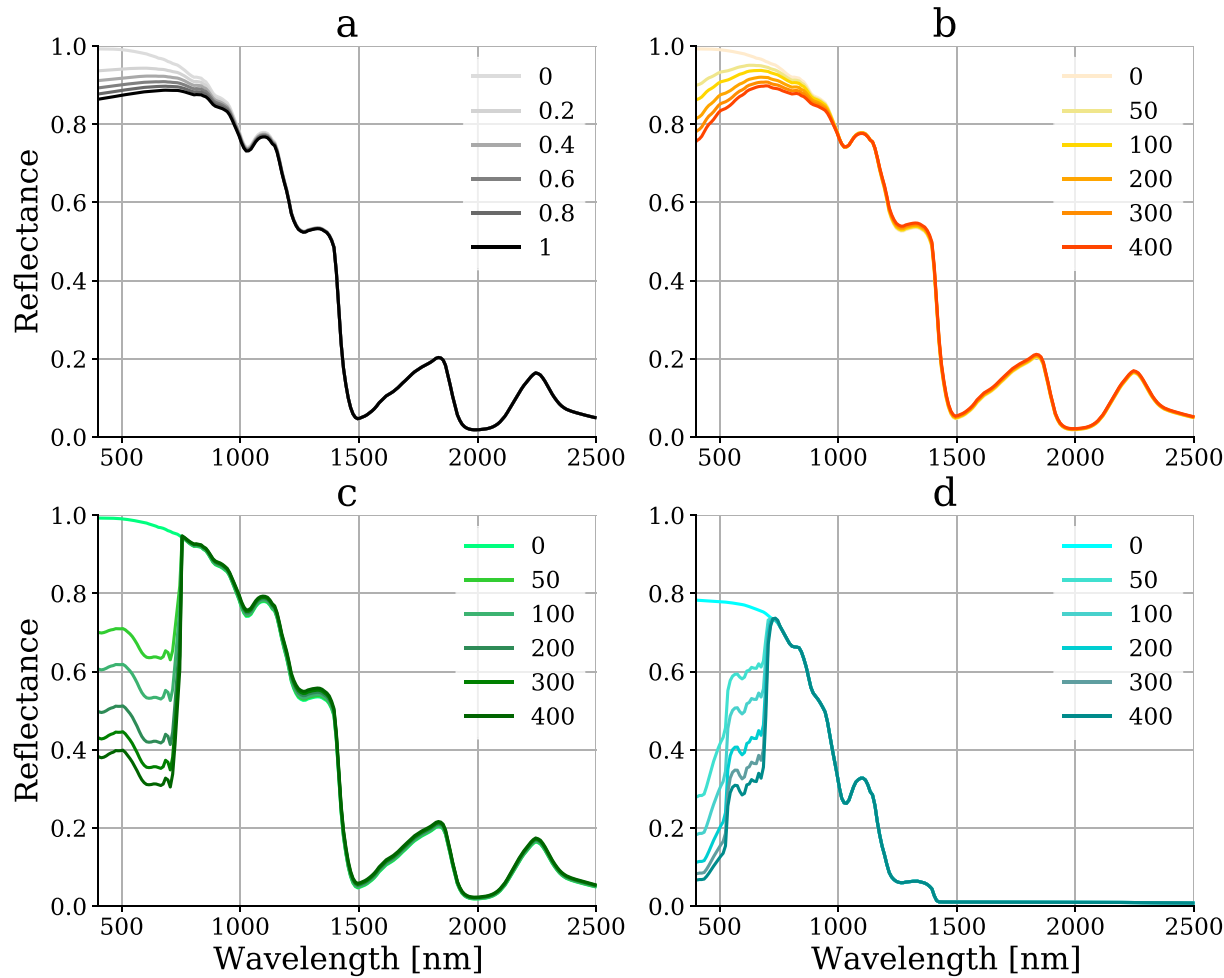


Fig. 2. Snow and ice surface reflectance including different LAP with varying mass mixing ratios in $\mu\text{g/g}_{\text{snow/ice}}$ modeled using BioSNICAR-GO. a) BC; b) mineral dust; c) snow algae; d) glacier algae. a) - c) are modeled for a snow grain radius of $100 \mu\text{m}$; d) for an ice crystal side length and diameter of $5000 \mu\text{m}$.

about $1500 \mu\text{m}$ for very wet snow (Painter et al., 2013; Green et al., 2002). For ice crystal dimensions, we chose the value range available in BioSNICAR-GO due to the lack of field observations. The liquid water fractions were selected according to the simulations in Green et al. (2002). For snow and glacier algae, we defined maximum values following field measurements performed by Painter et al. (2001) and Cook et al. (2020), respectively. Finally, the range of inorganic LAP was guided by observations of BC concentration presented in Flanner et al.

(2007), and by measurements of dust concentration from the Greenland Ice Sheet used in Cook et al. (2020). As our study focuses on ice surfaces on the Greenland Ice Sheet and uses the field measurements from Cook et al. (2020) for validation, we followed their parameterization of the ice layer physical properties having five layers of thicknesses between 0.1 and 1 cm ; underlying surface albedo of 0.15 ; and layer densities between 500 and 600 kg m^{-3} . Cook et al. (2020) selected this particular parameterization for the radiative transfer modeling as it reduces the

discrepancy of simulated spectra without any impurities to the mean field-measured clean-ice spectrum from the Greenland Ice Sheet. The simulations sum up to a comprehensive collection of reflectance spectra with sample mean \mathbf{x}_s and covariance \mathbf{S}_s , which serve as prior surface statistics.

Figs. 1 and 2 show some selected examples of reflectance spectra drawn from the collection of prior surface statistics. They evidence that our simulations capture typical spectral characteristics of snow and ice surfaces. The reflectance decreases with increasing snow grain size as shown by Fig. 1a. Wet snow not only shows a lower reflectance but also broader convolved ice and water absorption features that open to shorter wavelengths (Green et al., 2002) (Fig. 1b). Side lengths and diameters of hexagonal columnar ice crystals can be more than 10 mm (Cook et al., 2020), having a significant effect on the glacier ice reflectance (Fig. 1c).

Fig. 2 illustrates the effects of LAP on snow and ice surface reflectance. It is obvious that absorption due to LAP primarily occurs in the VIS. A mass mixing ratio of 1 $\mu\text{g}/\text{g}_{\text{snow}}$ BC can lead to a similar reduction in reflectance as a two orders of magnitude higher ratio of mineral dust (Fig. 2a - b). However, this depends entirely on the optical properties of BC and dust, which have enormous variability and for which no consensus has been reached yet how to accurately model and measure them (Skiles et al., 2017; Tuzet et al., 2019, 2020). Biological impurities in snow and ice can be classified into different species (Cook et al., 2020). On snow surfaces, unicellular *Chlamydomonas nivalis* are most dominant (Painter et al., 2001). They show unique chlorophyll-a and b absorption features at 680 nm as well as a broad carotenoid feature (Fig. 2c). On ice surfaces, such as the Greenland Ice Sheet, the algal occurrence is mainly controlled by *Mesotaenium berggrenii* and *Ancylonema nordenskioldii* (Yallop et al., 2012). Here, the main driver of absorption is a purple pigment having similarities to purpurogallin (Stibal et al., 2017), whose effect on the spectral shape of the ice reflectance is shown in Fig. 2d.

We apply a similar refinement to the prior statistics as Thompson et al. (2018). To allow the retrieval to match shapes outside the library subspace, we numerically regularize \mathbf{S}_s by adding the product of the identity matrix \mathbf{I} and a small value $\alpha = 10^{-6}$. To model non-Gaussian behavior, we first cluster the spectra into small groups and then fit a Gaussian distribution to each group independently (Funk et al., 2001). A small number of 8 components sufficiently improves the prior representation of the surface. We associate each cluster with mean \mathbf{x}_j and covariance \mathbf{S}_j with $j = \{1, \dots, 8\}$.

Throughout the optimization, the algorithm assigns the current \mathbf{x}_{SURF} to its closest cluster by minimizing the Mahalanobis distance $d(j)$ to \mathbf{x}_j accounting for \mathbf{S}_j :

$$d(j) = (\mathbf{x}_{\text{SURF}} - \mathbf{x}_j)^T \mathbf{S}_j^{-1} (\mathbf{x}_{\text{SURF}} - \mathbf{x}_j) \quad (14)$$

Thus, the appropriate surface mean and covariance to be considered for Eq. (2) are selected. To avoid constraints on the reflectance magnitude, we scale the chosen \mathbf{x}_j and \mathbf{S}_j by the norm of \mathbf{x}_{SURF} , z and z^2 , respectively.

2.3. Optimization

The optimization generally requires a first guess solution for the state vector parameters. The better the initial solution the more stable the inversion, which leads to fast convergence (Thompson et al., 2018). We start each iteration with the result from a band ratio retrieval for x_{H2O} using instrument channels located around 870, 900, and 940 nm (after Guanter et al. (2008)). For x_{AOT} , we use the prior mean as first guess. The resulting initial solution for \mathbf{x}_{ATM} is used to algebraically invert Eq. (11) to solve for a first estimate of $[x_{\lambda 1}, \dots, x_{\lambda m}]$. For $[x_{\text{SURF}1}, \dots, x_{\text{SURF}n}]$, we also take the prior mean.

The objective of the optimization is to find the maximum probability solution state $\hat{\mathbf{x}}$. We equate the first derivative of the right side of Eq. (2)

to zero. Since the derivative or gradient of our forward model is equivalent to its Jacobian, the following implicit equation for $\hat{\mathbf{x}}$ must be solved numerically (Rodgers, 2000):

$$-\hat{\mathbf{K}}^T \mathbf{S}_e^{-1} (\mathbf{y} - \mathbf{f}(\hat{\mathbf{x}})) + \mathbf{S}_a^{-1} (\hat{\mathbf{x}} - \mathbf{x}_a) = 0, \quad (15)$$

where $\hat{\mathbf{K}}$ is the Jacobian of the forward model with respect to $\hat{\mathbf{x}}$. In other words, Eq. (15) is used to find the zero of the gradient of Eq. (2). We use the Gauss-Newton iteration scheme as a numerical method to find $\hat{\mathbf{x}}$, which satisfies Eq. (15) (see Rodgers (2000)). If the problem is not too non-linear, the Newtonian iteration lets Eq. (15) converge to zero and the estimated $\hat{\mathbf{x}}$ leads to a global minimum of Eq. (2). This is especially the case if the cost function is exactly or nearly quadratic in \mathbf{x} . Of course, one could think of inherent noise in \mathbf{x} and \mathbf{y} , and of the associated effects on the numerical method used to solve Eq. (15). There might be the case that the iteration does not lead to convergence at zero and a further investigation of different numerical optimization methods would be necessary as part of future work. However, we found the Gauss-Newton scheme to be sufficient for our application as long as the starting point of the iteration is close to the solution. Details on the Gauss-Newton method and the convergence criterion we apply to stop the iteration are presented in Appendix A. The optimization usually converges in less than 30 iterations.

3. Materials

This section introduces the imaging spectroscopy data we use to evaluate the performance of the presented algorithm. First, we present the workflow to simulate EnMAP data, which serve as a basis for the sensitivity analysis (Section 3.1). Subsequently, Section 3.2 shortly presents the dataset of field observations collected on the Greenland Ice Sheet in July 2017, which we use to validate our results. Finally, Section 3.3 introduces the chosen AVIRIS-NG acquisition, likewise from the Greenland Ice Sheet.

3.1. Synthetic EnMAP data

We simulated EnMAP-like TOA radiance spectra of snow and ice surfaces with known grain size, liquid water fraction as well as LAP type and mass mixing ratio using a coupling of BioSNICAR-GO and the sensor model EnMAP end-to-end Simulation tool (EeteS) (Segl et al., 2012).

EnMAP is a push-broom imaging spectrometer scheduled for launch in 2022 with a mission lifetime of 5 years. The scientific preparation of the mission is led by the GFZ German Research Centre for Geosciences and should lead to Level 2A and 3 products designated for distribution under an open data policy (Guanter et al., 2015). EnMAP will move in a sun-synchronous orbit equipped with two cameras: a VIS/NIR camera covering 420 – 1000 nm with a mean SSI of 6.5 nm and a SWIR camera spanning 900 – 2450 nm with a mean SSI of 10 nm. The instrument is designed to have a swath width of 30 km and a ground sampling distance (GSD) of 30 m.

3.1.1. Modeling at bottom-of-atmosphere

We built collections of simulated reflectance spectra for two surface categories: snow and glacier ice. For both surfaces we set the same layer physical properties as for the simulation of the prior reflectance statistics (see Section 2.2.3). Likewise, we used the same types of BC and mineral dust as described in Section 2.2.3. We simulated snow spectra based on Mie modeling with grain radii ranging from 100 to 1500 μm , liquid water coatings in fractions between 0 and 25%, and various mass mixing ratios of snow algae, BC, and mineral dust.

The simulation of glacier ice spectra was based on the GO approach, for which we used ice crystal side lengths and diameters ranging from 5000 to 30000 μm and various mass mixing ratios of the glacier algae *Mesotaenium berggrenii* and *Ancylonema nordenskioldii*. We consciously chose comparatively large ice crystal dimensions for the GO modeling to

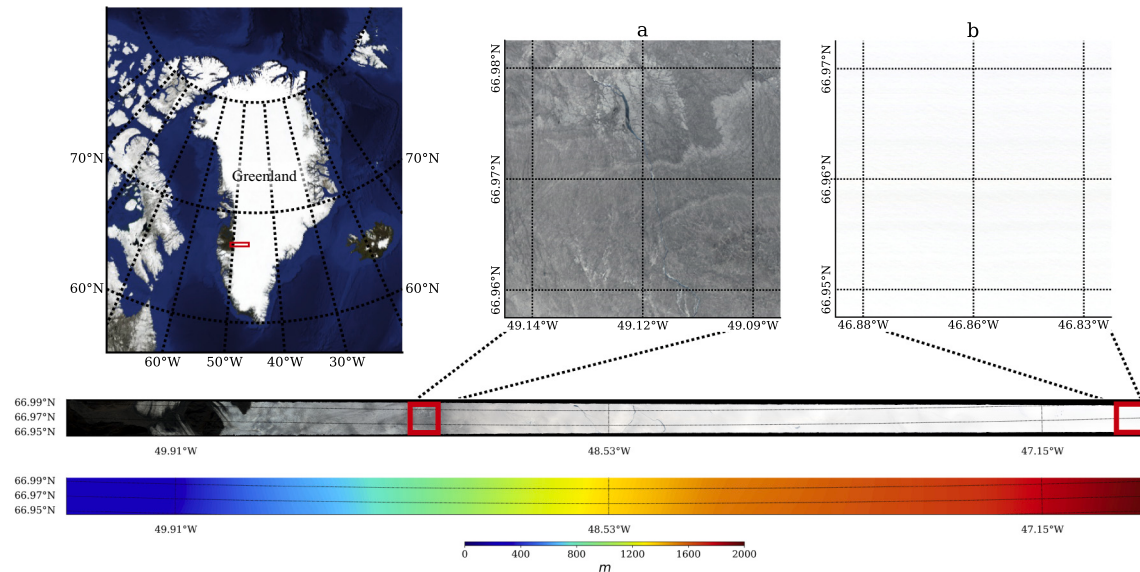


Fig. 3. Map of Greenland showing the AVIRIS-NG flightline as a red box (upper left panel) and a true-color image of the flight line with a map of the corresponding surface elevation in m (lower panel). The red boxes in the flightline indicate the locations of the subsets covering a) the lower lying dark ice and b) the higher elevated snow surface (upper right panel). (For interpretation of the references to color in this figure legend, the reader is referred to the web version of this article.)

better match the surface characteristics of melting ice sheets (see Cook et al. (2020)). Here, we abstained from incorporating inorganic LAP to reduce the complexity of the prior surface statistics. However, our simulation of snow spectra considers various BC and dust mass mixing ratios, which change the effect of a simultaneously present algae concentration. We acknowledge that this needs to be further validated with field measurements in order to better evaluate the influence of surface BC or dust on glacier algae retrievals.

3.1.2. Modeling at top-of-atmosphere

The two datasets of snow and ice surface reflectance spectra served as input for EeteS to calculate synthetic EnMAP TOA radiance. This tool simulates the entire final EnMAP product including a processing chain, which starts with the initial image data acquisition, provides radiometrically corrected Level-1B and orthorectified Level-1C data, and finally calculates atmospherically corrected Level-2A data. In-depth details about EeteS can be found in Segl et al. (2012).

Since the modeled datasets consist of a collection of reflectance spectra without any spatial reference, we only perform a simulation of spectral and radiometric characteristics assuming a pixel size of 30 m . The atmospheric simulation within EeteS is based on the MODTRAN code and we used identical viewing geometry and physical parameters for all snow and ice reflectance spectra ($VZA = 0^\circ$, $SZA = 40^\circ$, $RAA = 177^\circ$, $HSF = 0.1 \text{ km}$, $AOT = 0.2$, rural aerosol model). Only CWV was varied between 1.0 and 2.0 g cm^{-2} since its absorption overlaps the ice absorption features so that a closer look at the sensitivity of the algorithm to varying CWV concentration was necessary. To produce a synthetic dataset close to reality we simulated instrument noise with EeteS based on coefficients of a parametric noise model (Guanter et al., 2015). We used these coefficients to calculate radiance-dependent additive noise for each of the simulated TOA radiance spectra. For the calculation of the measurement error covariance matrix S_y , we use the same model to calculate the spectral SNR as a function of TOA radiance at run time.

3.2. Field measurements

In addition to the sensitivity analysis on fully synthetic data, we use field observations from the Greenland Ice Sheet to validate the results of the retrieval algorithm. The field data include reflectance measurements conducted with an ASD (Analytical Spectral Devices, Colorado)

FieldSpec Pro 3 and laboratory measurements of glacier algae mass mixing ratios obtained from ice samples taken from within the viewing area of the ASD. The data were collected and provided by Cook et al. (2020) in the frame of the Black and Bloom Project and were sampled from a Greenland field site at 67.04°N and 49.07°W between 10 and 17 July 2017.

The ASD was used to measure both the albedo and the HCRF from nadir view. A detailed description of the measurement protocol is provided in Cook et al. (2017a). We took the ASD HCRF spectra as input for the atmospheric and sensor simulations performed by EeteS to come up with TOA radiance in EnMAP dataformat. We used the same model parameters as described in Section 3.1.2. This step is necessary as the OE retrieval framework presented in this study requires TOA radiance spectra as input, so that a simultaneous retrieval of atmospheric and surface parameters is enabled.

To estimate glacier algae mass mixing ratios, Cook et al. (2020) investigated the ice samples by microscopic analyses in a laboratory. Based on the morphology of the cells they were separated into the two species *Mesotaenium berggrenii* and *Ancylonema nordenskioldii*. Total biovolume for each sample was then calculated by using measurements of the cell dimensions, the number of cells for each species, and an average cell volume. We followed the description in Cook et al. (2020) to convert biovolume to mass mixing ratio by multiplying the total average cell volume first by a constant cell density of 0.87 g cm^{-3} , then by the total number of cells/ mL for each sample, and finally by multiplying by the weight of 1 mL of ice (0.917 g). We use the resulting mass mixing ratios to validate the values obtained from the retrieval algorithm.

3.3. AVIRIS-NG measurements

To demonstrate the ability of the algorithm to realistically map snow and ice surface parameters we chose a dataset of real imaging spectroscopy measurements. We selected an AVIRIS-NG image acquired over the Greenland Ice Sheet on 31 August 2019 and chose two subsets of the flightline: one capturing a dark ice surface at an elevation of around 900 m at 66.97°N and 49.12°W , and another one covering a snow surface in a higher elevated region of around 2000 m with center coordinates 66.96°N and 46.86°W (Fig. 3). This selection was driven by our aim to show the differences in surface composition for dark ice and white snow, and to assess the influences of liquid water and glacier algae

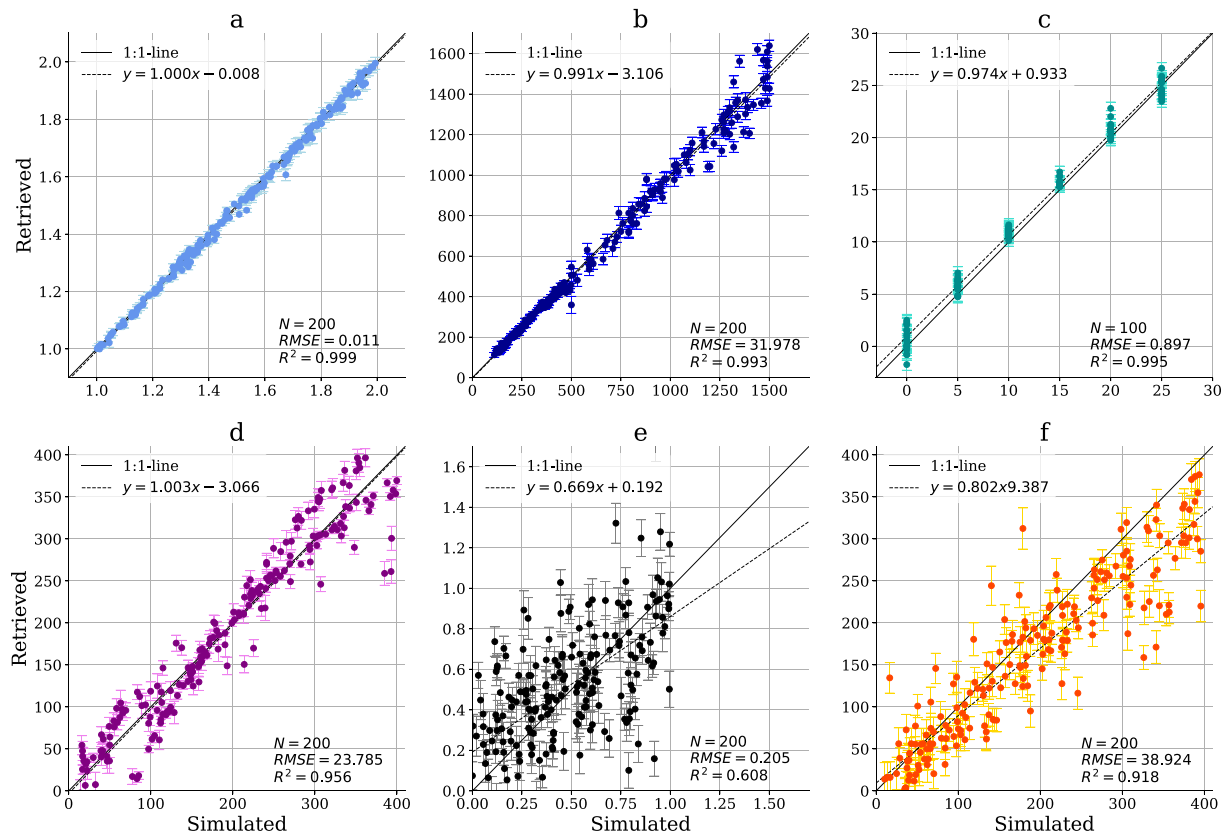


Fig. 4. Comparison of retrieved atmospheric water vapor and surface state parameters with the simulation input for the snow case. a) Water vapor [g cm^{-2}]; b) snow grain radius [μm]; c) liquid water fraction [%]; d) snow algae *Chlamydomonas nivalis* [$\mu\text{g/g}_{\text{snow}}$]; e) BC [$\mu\text{g/g}_{\text{snow}}$]; f) mineral dust [$\mu\text{g/g}_{\text{snow}}$]. Error bars show the posterior predictive uncertainties.

accumulation on the reflectance characteristics of ice and snow surfaces.

The channels of AVIRIS-NG cover the 380 – 2500 nm wavelength range with an SSI of 5 nm and varying GSD due to different flying altitudes (Hamlin et al., 2011). It can be installed on the NASA ER-2 research aircraft so that AVIRIS-NG is able to acquire data from a height of up to 20 km, which results in a GSD of 20 m. The AVIRIS-NG noise-equivalent change in radiance for each instrument channel needed for the retrieval algorithm was calculated according to Thompson et al. (2018).

4. Results and discussion

4.1. Model sensitivity analysis

4.1.1. Posterior predictive uncertainties

We analyze the sensitivity of the extended surface model by comparing the values of the solution state vector elements with the simulation input. Scatter plots illustrate the performance of the algorithm for each surface parameter separated into the different simulated surface categories snow (Fig. 4) and glacier ice (Fig. 5). Error bars within the plots visualize the posterior predictive uncertainties calculated during the optimization.

First of all, the results for atmospheric water vapor from the snow spectra confirm the ability of the retrieval algorithm to decouple atmospheric and surface state by showing an RMSE of 0.01 g cm^{-2} and a mean posterior uncertainty of $\pm 0.01 \text{ g cm}^{-2}$ (Fig. 4a).

Furthermore, the grain radius posterior predictive uncertainties shown in Fig. 4b agree with model uncertainties estimated in previous studies or even outperform them (Nolin and Dozier, 2000; Painter et al., 2013). Compared with the Nolin/Dozier model, which has an uncertainty of $\pm 20 - 50 \mu\text{m}$ for grain radii of up to $900 \mu\text{m}$ (Nolin and Dozier,

2000), our study indicates uncertainties in the same range for grain radii of more than $500 \mu\text{m}$ ($\pm 22 - 42 \mu\text{m}$), but decreased retrieval errors for grain radii below $500 \mu\text{m}$ ($\pm 8 - 12 \mu\text{m}$).

Overall, grain size, liquid water fraction, and algae mass mixing ratio show a distinct correlation with the simulation input, which certainly depends in part on using the same model both for the forward simulation and the inversion. Otherwise, we observe a systematic structure in Fig. 4d, which can be related to the saturating nature of algal absorption. The inversion using the multivariate Gaussian treats the relationship between the state vector and reflectance as locally linear, but in case of large absorption, nonlinearity in x increases. To improve performance for nonlinear state vector parameters, one could use alternative representations such as $\log(\mu\text{g/g}_{\text{snow/ice}})$ instead of $\mu\text{g/g}_{\text{snow/ice}}$.

The inorganic LAP have higher posterior predictive uncertainties since they do not exhibit distinct absorption features such as those of algae or liquid water (Cook et al., 2017b). Instead, they cause a smooth decrease in reflectance in cases of higher mass mixing ratios, comparable with the absorption and scattering effects of atmospheric aerosols (see Fig. 2). Therefore, an accurate estimation of inorganic LAP concentration is more challenging.

In particular, the estimated BC mass mixing ratios show a higher RMSE of $0.20 \mu\text{g/g}_{\text{snow}}$. Here, the mean posterior predictive uncertainties range from ± 0.05 to $\pm 0.11 \mu\text{g/g}_{\text{snow}}$, meaning a relative uncertainty of up to 100% for some BC retrievals (Fig. 4e). This decreased performance can be explained by the coincidence of a relatively high BC sensitivity of the surface reflectance in the VIS but significantly lower observable BC concentrations than other inorganic LAP can show (see Fig. 2). Consequently, even very low BC mass mixing ratios cause absorption in the VIS but could be overlaid with the absorption of higher concentrated LAP, such as dust and algae. Ultimately, the relative spectral invariance of BC absorption can lead to degeneracy with variation in absorption by

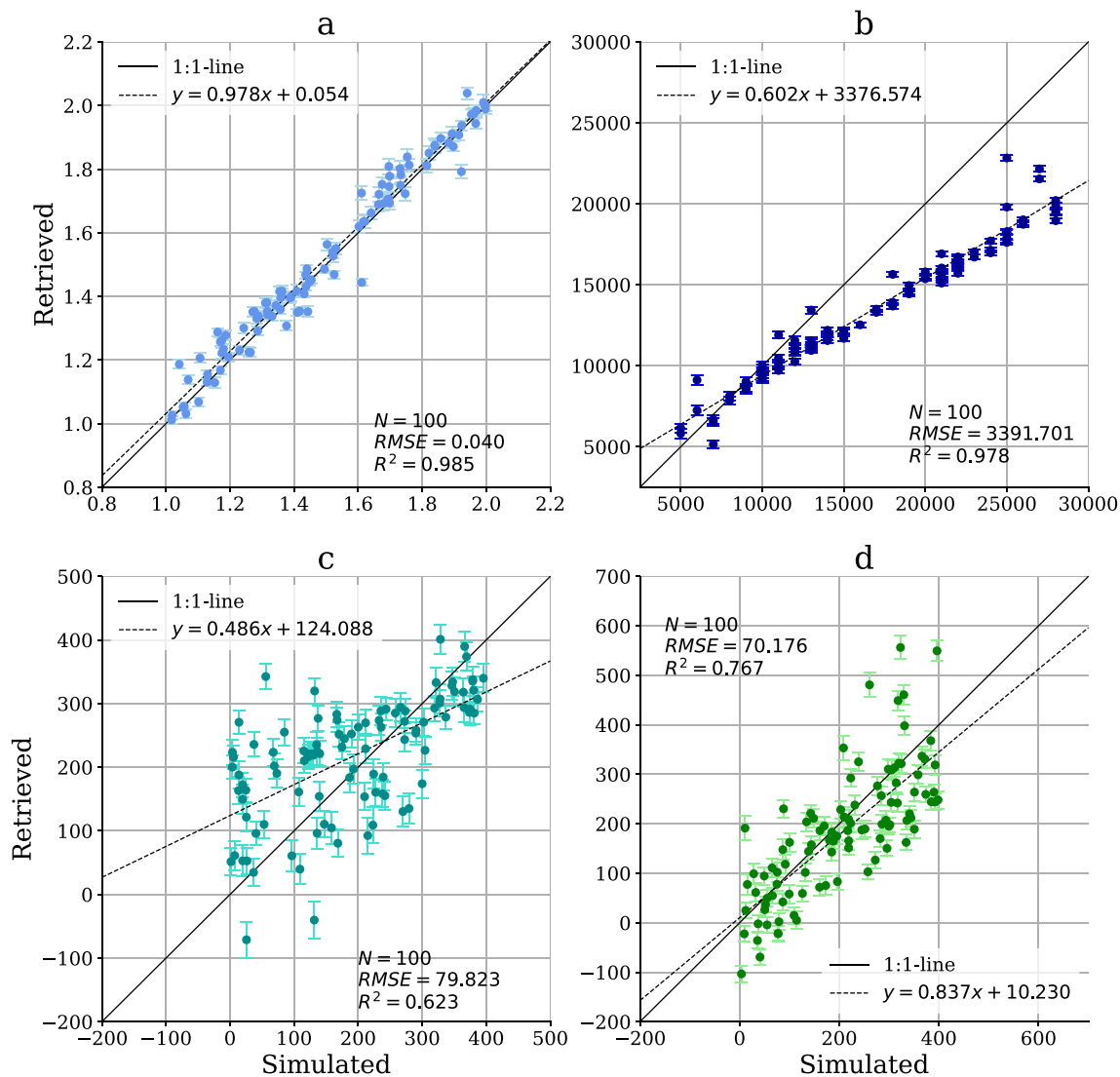


Fig. 5. Comparison of retrieved atmospheric water vapor and surface state parameters with the simulation input for the glacier ice case. a) Water vapor [g cm^{-2}]; b) ice crystal side length and diameter [μm]; c) glacier algae *Mesotaenium berggrenii* [$\mu\text{g/g}_{\text{ice}}$]; d) glacier algae *Acyanlonema nordenskioldii* [$\mu\text{g/g}_{\text{ice}}$]. Error bars show the posterior predictive uncertainties.

other LAPs.

Finally, the retrieval performance of dust LAP, which tend to be underestimated in our analysis (Fig. 4f), will strongly depend on the knowledge of actual dust optical properties. Skiles et al. (2017) and Skiles and Painter (2018) have shown with a novel optical property retrieval that the SNICAR dust can markedly be different from geographically varying dust and that what has been quantified in the field in impacting radiative forcing.

The retrieval of glacier ice surface parameters performs differently. Estimated ice crystal dimensions are correlated with the simulation input but clearly underestimated for values larger than $10000 \mu\text{m}$ (Fig. 5b). As previously illustrated in Fig. 1, the decrease in reflectance magnitude weakens with increasing ice crystal size. This impedes an accurate estimation of larger dimensions. Furthermore, models of glacier ice coincide less with assumptions about radiative transfer theory than models for snow reflectance. While snow is treated as a transparent medium in terms of air with a collection of scatterers that are also absorptive, glacier ice models deal with an absorbing medium with collections of both absorptive and transparent scatterers, e.g., enclosed air bubbles.

Another source of inaccuracy is the separated optimization of two

types of glacier algae, which leads to lower R^2 values of 0.62 and 0.77, respectively (Fig. 5c and d). *Mesotaenium berggrenii* and *Acyanlonema nordenskioldii* have very similar absorption features with only marginal differences. Hence, we propose to optimize the sum of both mass mixing ratios in order to achieve more accurate retrieval results. Nevertheless, the results — especially for *Acyanlonema nordenskioldii* — are still in an acceptable range and underline the capability of the lazy prior-driven inversion to recognize even small absorption differences based on the prior surface statistics.

4.1.2. Posterior error correlation

Next, we take a closer look at the posterior error correlation of the solution state. The $\hat{\mathbf{S}}$ matrix not only provides an estimate of the retrieval uncertainties but also information about the correlation between posterior errors of different state parameters. Govaerts et al. (2010) introduced a method to normalize $\hat{\mathbf{S}}$ so that a direct interpretation of the error correlation is enabled. This rescaling transforms $\hat{\mathbf{S}}$ into an error correlation matrix providing the correlation coefficients between the posterior predictive uncertainties of the state vector parameters.

Fig. 6 presents error correlation matrices for the two surface types

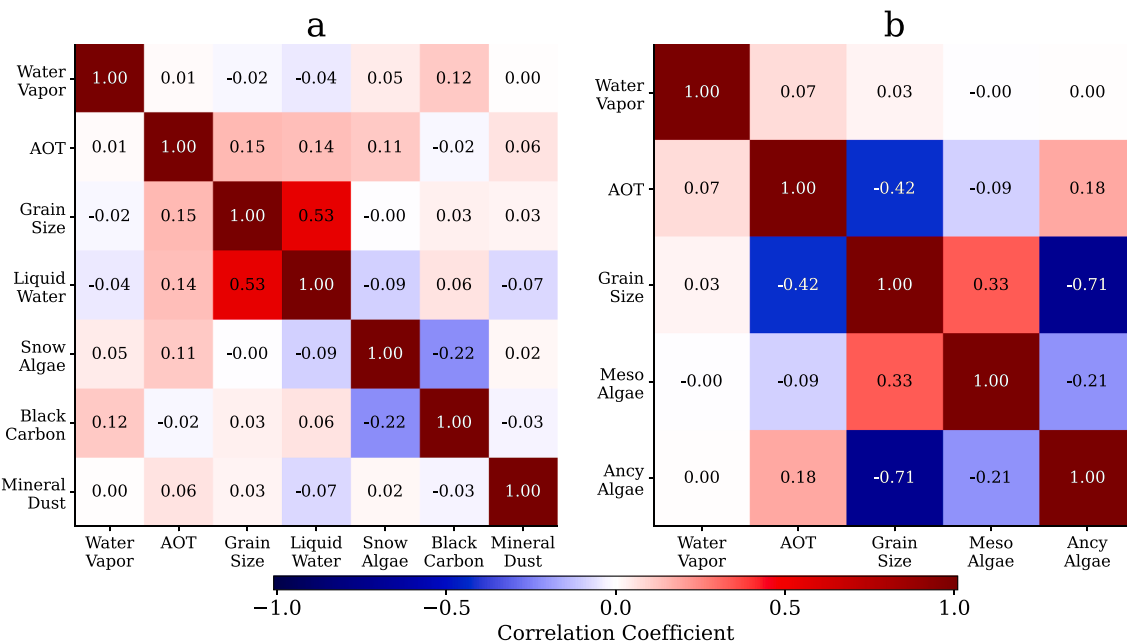


Fig. 6. Correlation error matrices for the atmospheric and surface state parameters except for the surface reflectance, calculated for the two different surface types. a) Snow; b) glacier ice.

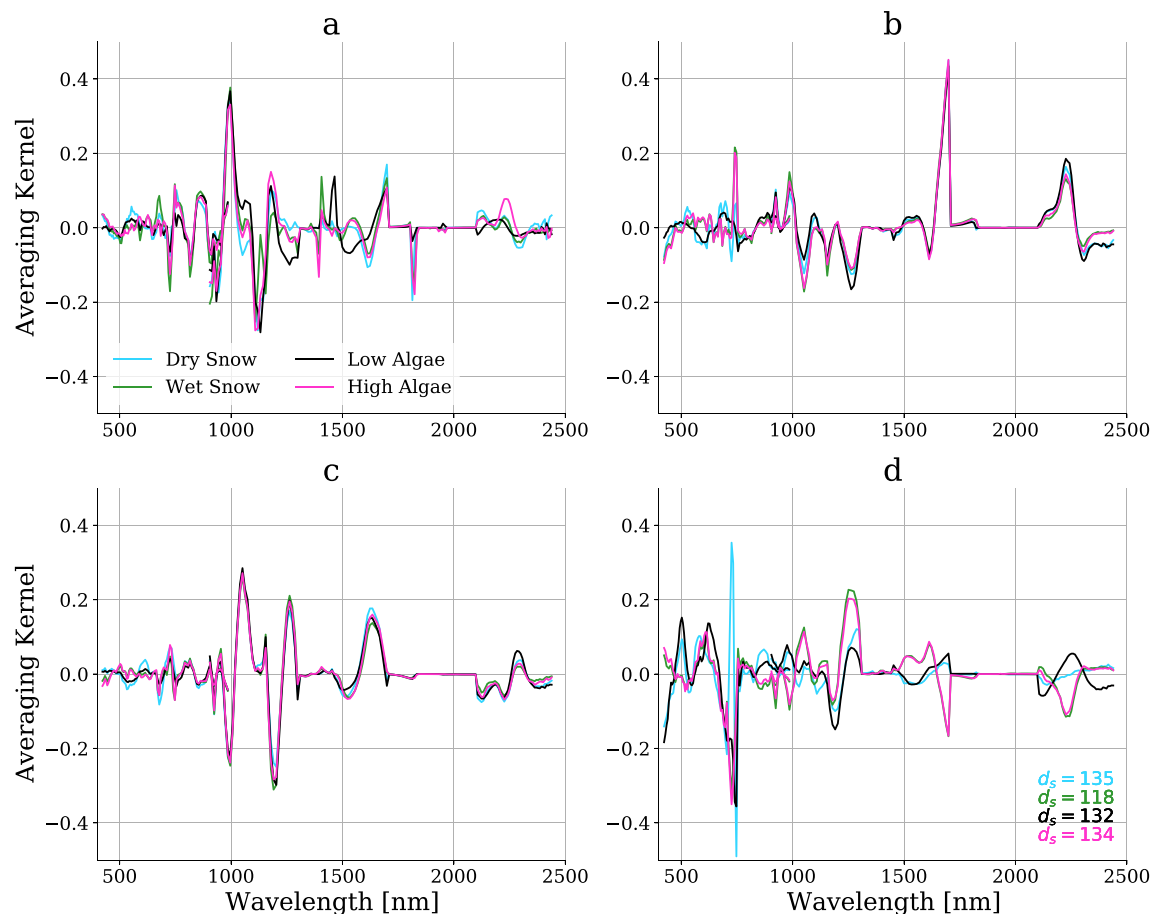


Fig. 7. Normalized averaging kernels from the sensitivity analysis for selected surface conditions. a) Water vapor; b) snow grain size; c) liquid water fraction; d) algae mass mixing ratio. The additional legend in panel d) shows the total degree of freedom d_s for each surface.

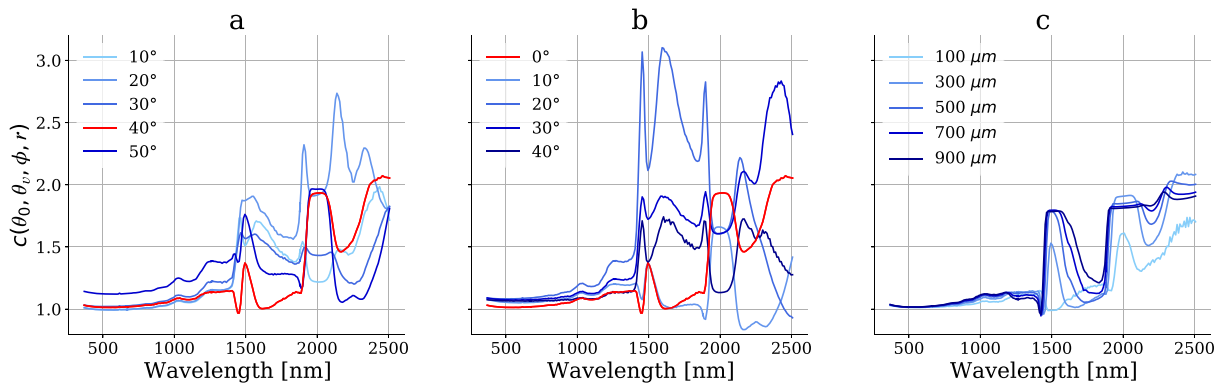


Fig. 8. Spectral anisotropy factor as a function of a) SZA with fixed snow grain radius = 250 μm , VZA = 0°, RAA = 0°; b) VZA with fixed snow grain radius = 250 μm , SZA = 40°, RAA = 0°; c) snow grain radius with fixed SZA = 40°, VZA = 0°, RAA = 0°. (For interpretation of the references to color in this figure legend, the reader is referred to the web version of this article.)

from the sensitivity analysis, snow and glacier ice. The snow matrix clearly shows an independence between atmospheric and surface state since uncertainties in both water vapor and AOT are almost uncorrelated with all surface posterior errors. Retrieval uncertainties show a marginal correlation between water vapor and BC as well as between AOT and grain size, liquid water, and snow algae errors. This could simply be introduced by having a high number of surface state parameters. In contrast to that, the anticorrelation between estimation uncertainties of grain size and AOT for the glacier ice case can be explained by the decrease in reflectance magnitude caused by larger ice crystal dimensions. As this effect resembles the absorption caused by atmospheric aerosols, an underestimation of grain size could lead to an overestimation of AOT and vice versa. Furthermore, the matrix for the retrieval from snow spectra highlights the correlation between errors in the estimation of grain size and liquid water fraction, which might be caused by the only slightly shifted absorption lines of liquid water and ice (see Green et al. (2006); Bohn et al. (2020)).

4.1.3. Sensitivity to the true state

Fig. 7 shows normalized averaging kernels of water vapor, grain size, liquid water, and algae displayed for different simulated surface conditions. Overall, the sensitivity of the parameters to changes in the true state reflectance follows our expectations. Water vapor, liquid water, and grain size are most sensitive to reflectance changes in the water vapor absorption bands around 940 and 1140 nm, when excluding the saturated features in the SWIR, and the algae estimation can be biased especially through changes in the true VIS reflectance. The total degrees of freedom displayed in panel d) indicate a similar amount of information available in the spectra, except for the wet snow case. This suggests that larger grain sizes in combination with liquid water fractions decrease the number of retrievable variables above the measurement noise. Interestingly, this is not the case for high algae mass mixing ratios, leading to the assumption that the level of information content is almost independent from present algae concentrations.

All these findings imply the validity of the lazy prior-driven inversion to map additional surface parameters for snow and ice surfaces. However, the sensitivity analysis is based on synthetic EnMAP TOA radiance spectra excluding any spatial simulation. Therefore, we assume pixels with 30 m GSD without any influences of neighboring pixels or mixed surface types affecting the reflectance. Using real data, these effects could certainly have an impact on the retrieval accuracy.

4.1.4. Sensitivity to directional effects

As we use simulations of snow and ice spectral albedo in place of HDRF to build the prior surface reflectance statistics, this section illustrates the sensitivity of our approach to directional effects in the reflectance.

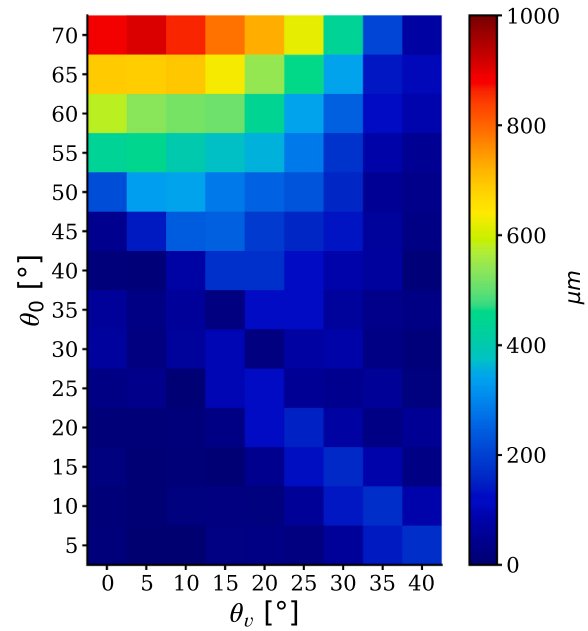


Fig. 9. Absolute retrieval uncertainty of snow grain radius as a function of varying solar and view zenith angles. The values are obtained by calculating the root-squared error between inferred and input snow grain radius after applying the spectral albedo-based retrieval framework to synthetic EnMAP TOA radiance spectra. The latter are generated from HDRF simulations with a constant input grain radius of 500 μm and RAA of 0°.

Based on a set of snow HDRF simulations processed with DISORT for varying solar and observation angles as well as snow grain radii, we calculate the anisotropy factor c according to Eq. (13). Fig. 8 shows the sensitivity of c to changing SZA, VZA, and grain radii, respectively. The snow anisotropy factor is closer to 1 for wavelengths below 1000 nm, especially for both small SZA and VZA. The sensitivity to increasing grain radii is also markedly smaller in the VIS and NIR spectrum, and only increases towards the SWIR. Fig. 8a and b demonstrate that even in the wavelength range between 1000 and 1500 nm the difference between spectral albedo and HDRF for the particular geometry we simulated in our study (SZA = 40°, VZA = 0°; depicted by the red lines) is less than 20%.

In order to exemplify the sensitivity of the retrieval algorithm to directional effects in the surface reflectance, we simulated EnMAP TOA radiance spectra based on a selected subset of HDRF simulations with SZA = {5°, ..., 70°}, VZA = {0°, ..., 40°}, and fixed snow grain radius of

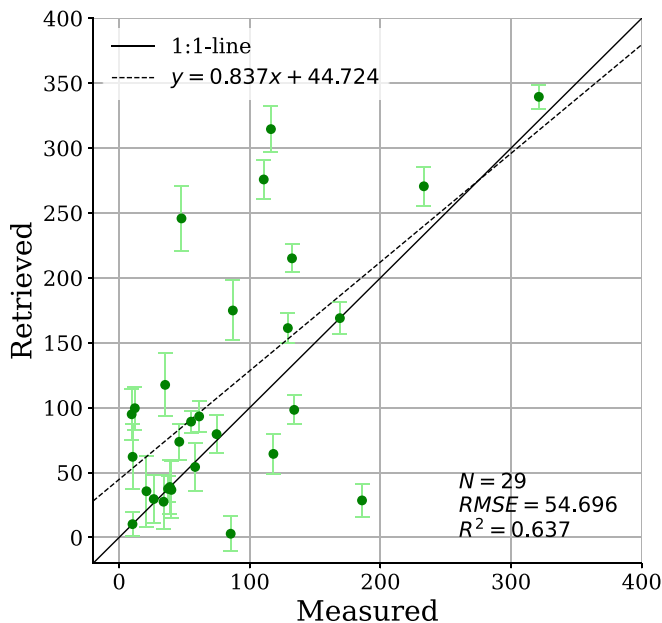


Fig. 10. Comparison of estimated glacier algae mass mixing ratio with the laboratory measurements in units of $\mu\text{g/g}_{\text{ice}}$. Error bars show the posterior predictive uncertainties.

500 μm and RAA of 0° . Then, we applied the retrieval framework using spectral albedo as prior statistics and calculated absolute retrieval uncertainties of snow grain radius (Fig. 9). Our results show that snow grain radius retrieval uncertainties significantly increase for SZA beyond 45° . Similarly, VZA larger than 10° lead to uncertainties of $\pm 100 \mu\text{m}$ and more if the solar zenith angle is at least 25° . However, we observe low uncertainties of $\pm 0 - 40 \mu\text{m}$ for SZA below 25° and VZA between 0° and 10° . The particular geometry used for our sensitivity analysis of SZA = 40° and VZA = 0° likewise shows a low uncertainty of $\pm 14.7 \mu\text{m}$. These values accord both with the estimated posterior predictive uncertainties presented in Section 4.1.1 and the Nolin/Dozier model (Nolin and Dozier, 2000).

Ultimately, these arguments justify the use of a simplified two-stream model such as BioSNICAR-GO for our case study, especially since the focus of this work is on the OE-based retrieval method rather than the radiative transfer modeling of snow itself. However, for the full implementation for airborne and spaceborne instruments that covers the SZA and VZA ranges of such programs, it is requisite that we use boundary condition spectral HDRF that incorporate the optical properties of the organics into the directional reflectance modeling.

4.2. Retrieval from field measurements

4.2.1. Validation with measurements of glacier algae

Cook et al. (2020) measured the mass mixing ratio of glacier algae separated into the species *Mesotaenium berggrenii* and *Ancylonema nor-denskioldii*. We use the summed concentrations to validate the values estimated by the lazy prior-driven inversion. Fig. 10 shows this information as a scatter plot. The result reports an R^2 of 0.64 and about one third of the samples being located on or close to the 1 : 1-line. However, the mean posterior predictive uncertainty of $\pm 16.4 \mu\text{g/g}_{\text{ice}}$ corresponds to a relative retrieval error of up to 50%. As visualized by Fig. 6, uncertain knowledge of other surface parameters can influence the retrieval accuracy of algal LAP. Therefore, improved studies of quantifying BC and dust optical properties will be mandatory to increase the retrieval accuracy of glacier algae concentration. Our analysis can be seen as one of the first approaches though to validate retrieved algae mass mixing ratios with in-situ measurements.

4.2.2. Averaging kernels

We again analyze selected averaging kernels for the field validation. Fig. 11 illustrates the normalized sensitivity to the true state reflectance of retrieved water vapor, snow grain size and ice crystal dimension, liquid water fraction, and algae mass mixing ratio. We display four surface conditions which are determined based on our retrieval results: dry snow without algae, wet snow with low algae mass mixing ratio, large ice crystals with low algae concentration, and small ice crystals contaminated by a high algae loading. The averaging kernels show a similar behavior as those from the sensitivity analysis (see Fig. 7). Errors in water vapor, grain size, and liquid water estimation are most likely introduced through changes in the reflectance of the water absorption bands around 940 and 1140 nm. In contrast to that, algae mass mixing ratios are mainly sensitive to changes in the true VIS reflectance. It is notable that the total degrees of freedom vary much more than in the sensitivity analysis. Snow surfaces provide significantly more information than ice surfaces which are composed of crystals with considerably larger dimensions than snow grains typically have. As previously shown, large ice crystals not only increase the depth of the ice absorption features but also decrease the reflectance magnitude. Consequentially, the lower reflectance levels provide less retrievable information.

Nevertheless, the algorithm is able to accurately estimate different shapes and magnitudes of snow and ice surface reflectance (Fig. 12). We compare the values from the solution states with the ASD spectra which served as input for the simulated data (see Section 3.2). For all wavelengths, the residuals are below 2% except for the saturated SWIR water absorption features. However, small deviations in the estimated surface reflectance could also be caused by calibration errors or uncertainties due to measurement noise in the ASD instrument.

4.3. Retrieval from AVIRIS-NG measurements

4.3.1. Retrieval maps

In the following sections we finally present retrieval results from the selected AVIRIS-NG Greenland subsets. Fig. 13 shows surface parameter maps for snow grain size, ice crystal dimensions, liquid water fraction, and mass mixing ratios of snow and glacier algae. For the high elevated snow surface, the algorithm reports small grain sizes, no liquid water coatings around the snow grains and likewise no accumulation of snow algae on the surface. Here, the grain size map shows remarkable linear features emerging in west-east direction. They can be the direct cause of imperfect calibration of the radiance data and appear in the array spectrometer data at level 1a and 1b. In contrast, the dark ice surface with an elevation of around 900 m features large ice crystals with both accumulated liquid water and comparatively high glacier algae mass mixing ratios. Especially the estimated distribution of liquid water suggests active melt processes. This indicates the potential of the algorithm to exploit imaging spectroscopy measurements for supporting observations and the understanding of melting ice sheets.

4.3.2. Liquid water vs. glacier algae

A key finding from analyzing the AVIRIS-NG data is a significant positive correlation between the amount of available liquid water in-between the ice crystals and the occurrence of glacier algae. The need for addressing the relationships of algal concentration to snow and ice physical properties was already formulated in Painter et al. (2001) and plays an important role in understanding the impacts of algal blooms on the melting of the Greenland Ice Sheet (Yallop et al., 2012; Cook et al., 2017b, 2020). We analyze the estimated values for the western subset and present scatter plots for both liquid water fractions in percent and absolute liquid water sphere radius in μm accompanied with the respective prior mean glacier algae mass mixing ratios chosen from the surface statistics (Fig. 14). To reduce the complexity of the scatter plots and to generate spatially more robust values for comparison, we clustered the estimated glacier algae map into contiguous segments of nearly similar mass mixing ratios. We then took the same spatial segments to

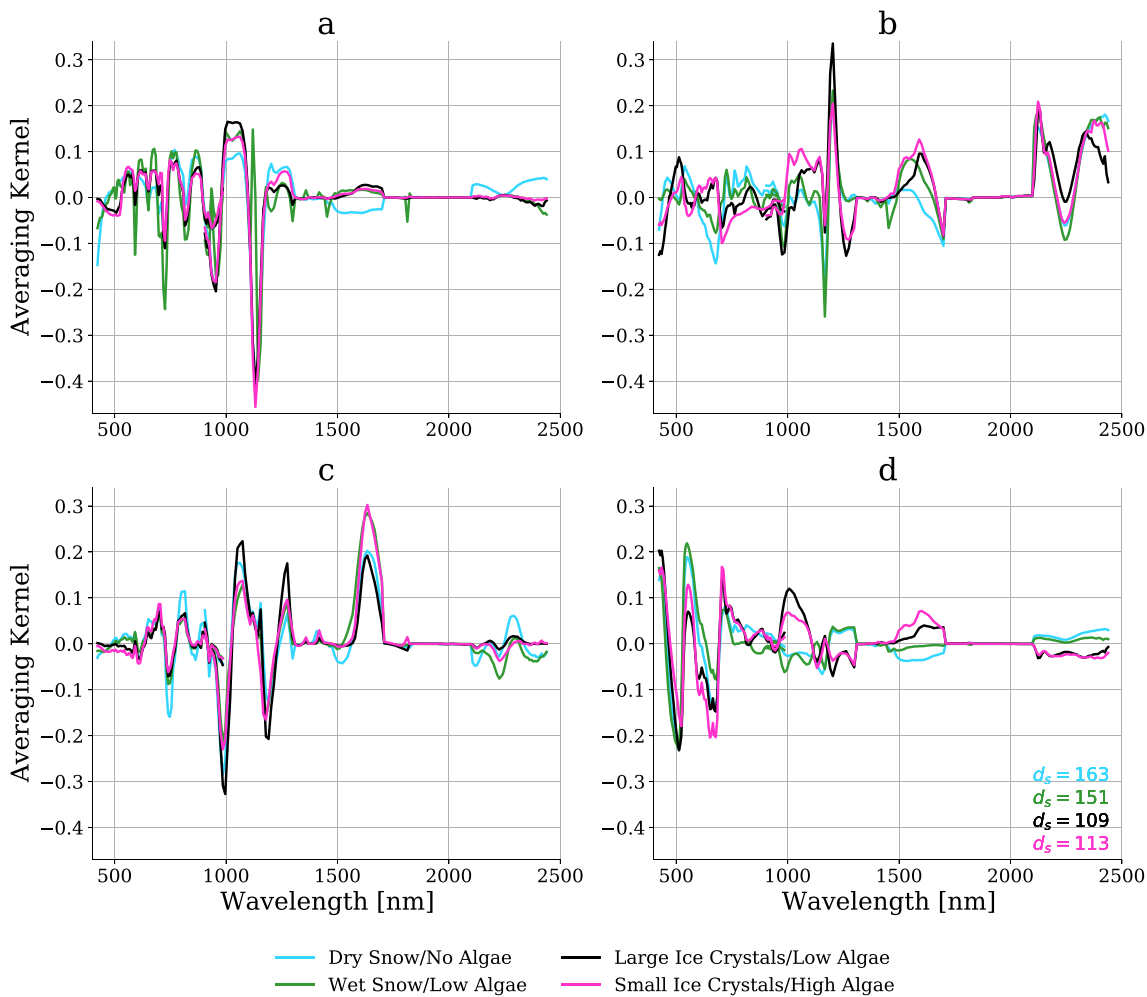


Fig. 11. Normalized averaging kernels from the retrieval based on the ASD field measurements for selected surface conditions. a) Water vapor; b) snow grain size/ice crystal side length and diameter; c) liquid water fraction; d) algae mass mixing ratio. The additional legend in panel d) shows the total degree of freedom d_s for each surface.

cluster the remaining retrieval maps and the prior mean and compare the average values from each segment. While we observe an R^2 of 0.76 for the correlation with liquid water fraction, the glacier algae accumulation seems to be likewise correlated with the absolute amounts of liquid water coated around the ice crystals having an R^2 of 0.64. Overall, our results support the assumption of the positive glacier algae-liquid water feedback mentioned in Williamson et al. (2018) and Dial et al. (2018). Both studies report a high probability that the accumulation of glacier algae leads to increased melt due to enhanced radiative forcing. The successive generation of liquid water releases nutrients in-between the ice crystals, which further stimulates glacier algal growth. These nutrients can originate from deposited mineral dust introducing a feedback even between inorganic LAP and glacier algae (Sibal et al., 2017). The causal interpretation of Fig. 14 could just as easily be inverted, with increased glacier algal mass mixing ratios causing higher liquid water fractions. Fig. 14 also confirms the performance of the surface model as values of prior and solution state of glacier algae mass mixing ratio show a distinct accordance. We observe that the prior assumption is already close to the solution demonstrating that the pre-calculated statistical relationships between the surface components capture the solution state.

4.3.3. Estimated surface reflectance

Finally, Fig. 15 shows estimated surface reflectance spectra from the lazy prior-driven inversion and the ATREM code, which is currently

applied for generating the official AVIRIS-NG L2A data products (see Thompson et al. (2015)). We present results for a dry snow spectrum without significant absorptive influence of LAP as well as a spectrum of melting ice contaminated with a high algae mass mixing ratio. Both examples confirm a match between the two atmospheric correction methods, which leads to the assumption that the lazy prior-driven inversion is suited to estimate snow and ice surface reflectance by drawing upon the simulated surface prior statistics. We did not exclude reflectance values from instrument channels located within the deep SWIR water vapor absorption features so that some spikes, e.g., around 1350 nm remain. The atmosphere is almost opaque at these wavelengths and even some marginal errors in the simulation of atmospheric water vapor transmission could lead to artificially high reflectance values. However, the performance of the presented inversion method is further corroborated by the fact that the ATREM code incorporates a three phases of water retrieval leading to an increased accuracy of the estimated surface reflectance (Green et al., 2006; Thompson et al., 2015; Bohn et al., 2020). Applied to snow and ice spectra this method smooths the ice absorption features around 1030 and 1250 nm, which are likewise captured by the lazy prior-driven inversion.

5. Conclusion

We present a new method to retrieve snow and ice surface parameters from imaging spectroscopy measurements. The retrieval exploits the

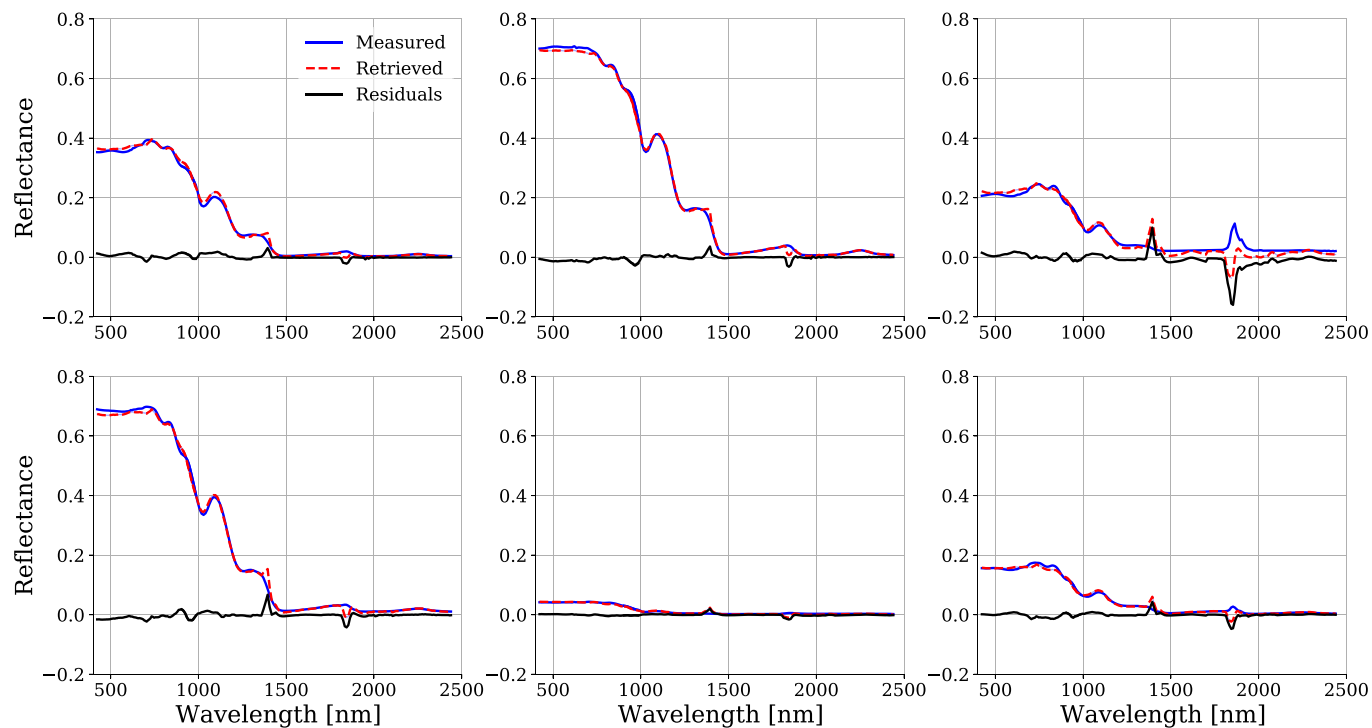


Fig. 12. Examples of estimated surface reflectance from the simulated EnMAP TOA radiance spectra based on the ASD field measurements.

statistical relationships between reflectance and snow grain size, ice crystal dimension, liquid water fraction as well as mass mixing ratio of various LAP by adopting an extended surface model. The framework of a simultaneous retrieval of atmospheric and surface parameters provides a novel rigorous propagation of uncertainties caused by instrument noise, unknown model parameters, and prior knowledge, through the retrieval chain up to a quantification of final level 3 product uncertainties. At the same time, this approach enables a detailed investigation of posterior error correlation between atmospheric and surface state parameters. We analyze the sensitivity of the algorithm based on synthetic EnMAP data and present a field validation using samples of ASD measured spectra with corresponding laboratory measurements of glacier algae collected on the Greenland Ice Sheet.

The sensitivity analysis demonstrates accurate estimation of surface properties both for snow and glacier ice. All snow parameters are retrieved with an R^2 of more than 0.90 and less than 0.8% posterior uncertainty, except for inorganic LAP such as BC and mineral dust. They show larger deviations between simulated and retrieved values since their spectral absorption features are less distinct. This makes an accurate estimation more challenging. The results from glacier ice spectra indicate that retrieval uncertainties increase with grain size since the reflectance magnitude significantly declines for larger ice crystal dimensions. This reduces the degrees of freedom and the information content provided by the measurement. In contrast, our analysis shows that the information content is almost independent from the occurrence of biological LAP, which is a promising basis for future investigations of algal blooms on snow and ice surfaces. Furthermore, the investigation of posterior uncertainty correlation between atmospheric and surface state parameters emphasizes that errors in the retrieval of atmospheric AOT can significantly bias the estimation of ice crystal dimensions on ice surfaces.

The validation with field observations is one of the first approaches to directly compare remotely retrieved snow or glacier algae concentrations with in-situ measurements. It yields promising results with an R^2 of 0.64 and a high retrieval accuracy for more than half of the samples. In addition, the algorithm precisely maps different shapes and magnitudes of surface reflectance spectra with less than 3% residuals.

Finally, we evaluate the algorithm with a case study of an AVIRIS-NG acquisition from the Greenland Ice Sheet. The retrieval reports likely expected value ranges and indicates active melt processes on dark ice surfaces. Furthermore, the results confirm a remarkable positive correlation between the amount of available liquid water in-between the ice crystals and the occurrence of glacier algae. This is in accordance with the positive algae-liquid water feedback described in previous studies and underlines the value of the presented method for improving the understanding of glacier ice melt processes.

In summary, our study demonstrates a promising potential to exploit imaging spectroscopy measurements for supporting observations of melting ice sheets. In this context, the lazy prior-driven inversion proves of value for estimating additional surface parameters based on prior statistics. It is a straightforward method, which serves as a prototype for future snow and ice surface property retrievals.

However, as our work uses simulations of spectral albedo in place of HDRF for the prior statistics, the consideration of directional reflectance from anisotropic surfaces will be an important part of future work. In particular, when transferring the algorithm to rough mountainous terrain and using off-nadir pointing capabilities of imaging spectrometers, the use of a multistream RTM such as DISORT to consider directional effects in the surface reflectance would be important to achieve accurate retrieval results.

Furthermore, mixed pixels are not accessible for accurate retrievals applying the method presented in this study. In contrast to most parts of the ice sheets, the remaining cryosphere mainly features a mixture of varying surface cover. Therefore, an upstream retrieval of snow subpixel cover will significantly decrease uncertainties when applying the algorithm to other regions than the Greenland Ice Sheet.

Finally, including a temporal component in the prior mean and covariance derivation could further improve the retrieval performance. For instance, simulations or measurements of snow and ice HDRF as a function of daytime and season would capture both short- and long-time variations due to alternating melt and freezing events.

Upcoming orbital imaging spectroscopy missions such as EnMAP and CHIME, and the anticipated SBG investigation, can address these issues by providing data on a regular basis with a global coverage and hence, a

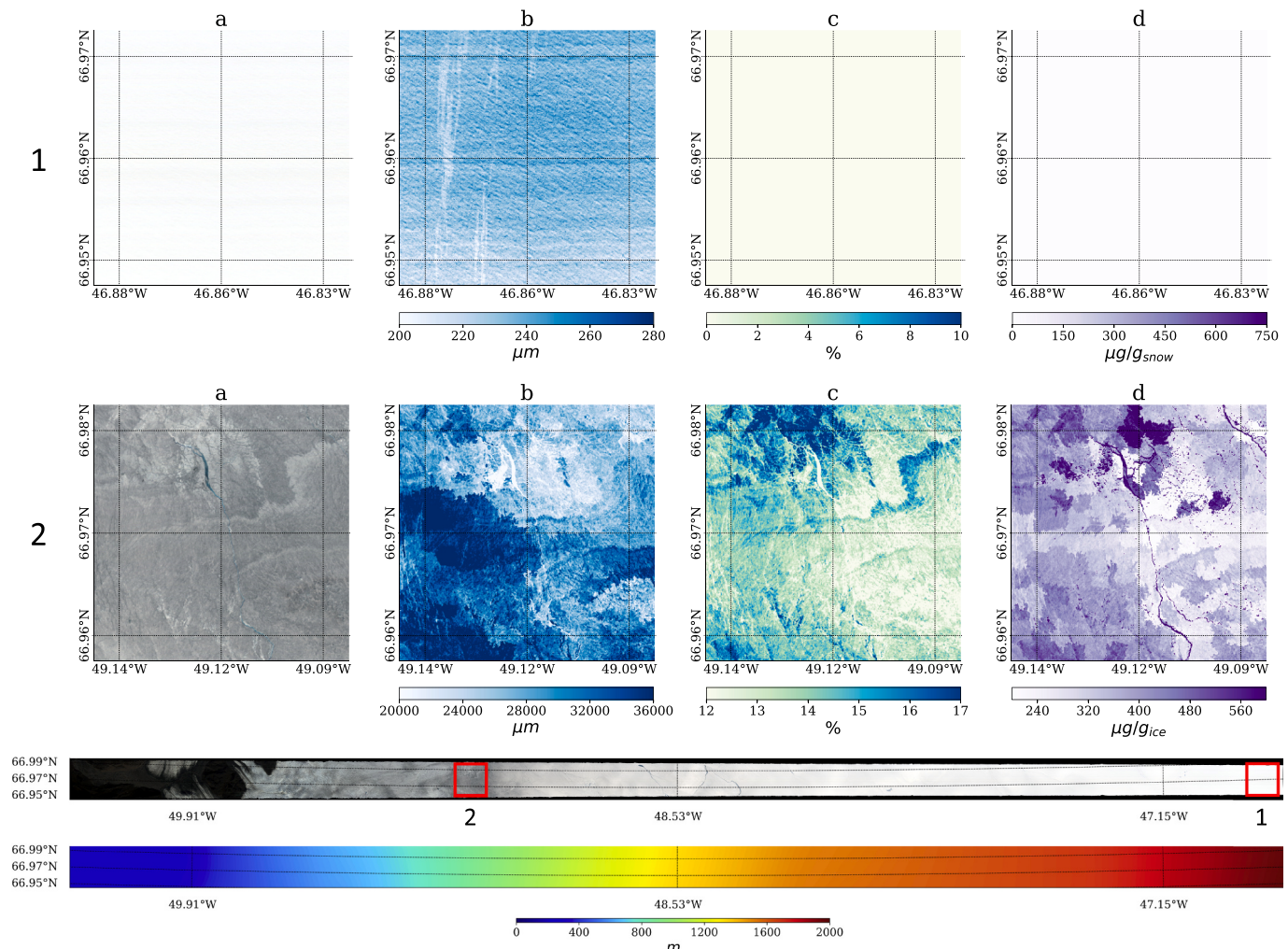


Fig. 13. Estimated surface parameter maps for the AVIRIS-NG snow and dark ice subsets. Upper panel: a) True-color image; b) snow grain radius; c) liquid water fraction; d) snow algae mass mixing ratio. Middle panel: a) True-color image; b) ice crystal dimension; c) liquid water fraction; d) glacier algae mass mixing ratio. The results are accompanied with a true-color image of the complete flight line with a map of the corresponding surface elevation in m (lower panel). The red boxes in the flight line indicate the locations of the subsets covering 1) the higher elevated snow surface and 2) the lower lying dark ice. (For interpretation of the references to color in this figure legend, the reader is referred to the web version of this article.)

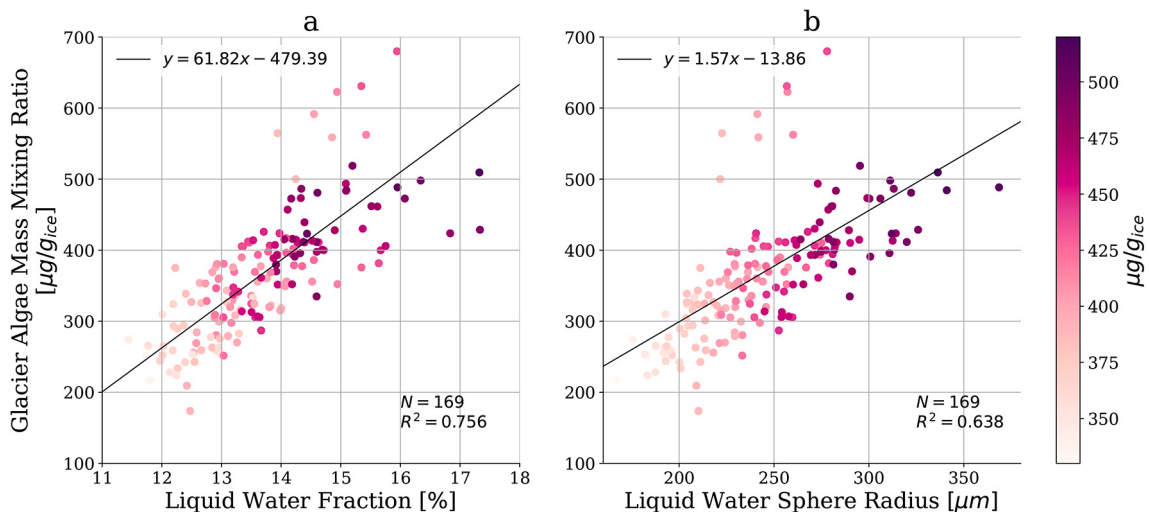


Fig. 14. Correlation between estimated glacier algae mass mixing ratio and a) liquid water fraction, and b) absolute liquid water sphere radius, for the AVIRIS-NG dark ice subset. The colormap shows the particular prior state value for the glacier algal LAP selected from the surface model.

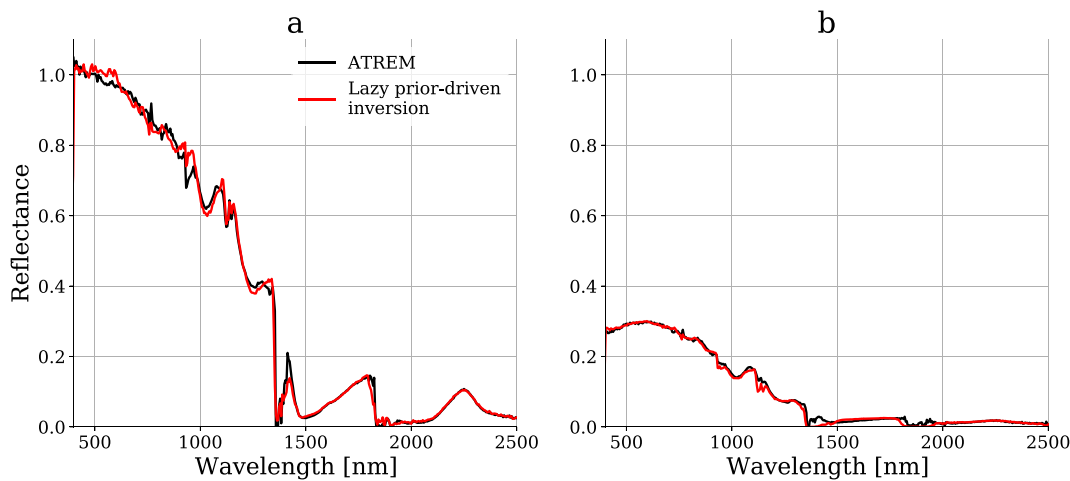


Fig. 15. Examples of estimated surface reflectance from the AVIRIS-NG radiance measurements calculated with the ATREM code and the lazy prior-driven inversion. a) Dry snow; b) melting ice contaminated with high algae mass mixing ratio.

valuable input for a transfer of the presented snow and ice parameter retrieval to more challenging surfaces.

Declaration of Competing Interest

The authors declare no conflict of interest.

Acknowledgments

This work has been done in the frame of EnMAP, which is funded under the DLR Space Administration with resources from the German

Federal Ministry of Economic Affairs and Energy (grant No. 50 EE 0850) and contributions from DLR, GFZ and OHB System AG. Joseph M. Cook was in part supported by a grant from the European Research Council (ERC) under the European Union's Horizon 2020 Research and Innovation Programme (ERC Synergy Grant 'Deep Purple'; grant agreement No. 856416) and the NERC Standard Grant 'MicroMelt', code NE/S001034/1. We acknowledge the support of a Jet Propulsion Laboratory Advanced Concepts grant. A portion of this research took place at the Jet Propulsion Laboratory, California Institute of Technology, under a contract with the National Aeronautics and Space Administration (80NM0018D0004).

Appendix A. Numerical optimization method

Compared with Newton's iteration scheme, the Gauss-Newton method does not require the calculation of second derivatives of the forward model, which can pose an elaborate challenge. The maximum a posteriori solution for $\hat{\mathbf{x}}$ can be written in the m-form, if the dimension of the measurement vector is smaller than the dimension of the state vector, or the n-form, which is the other way round. Since our state vector contains both reflectance values for each instrument channel and the additional atmospheric and surface parameters, its dimension is always larger than the number of elements in the measurement vector. Consequentially, we apply the m-form to find the most probable $\hat{\mathbf{x}}$ and update the solution state at iteration step $i + 1$ by:

$$\mathbf{x}_{i+1} = \mathbf{x}_a + \mathbf{S}_a \mathbf{K}_i^T (\mathbf{K}_i \mathbf{S}_a \mathbf{K}_i^T + \mathbf{S}_f)^{-1} (\mathbf{y} - \mathbf{f}(\mathbf{x}_i) + \mathbf{K}_i(\mathbf{x}_i - \mathbf{x}_a)), \quad (A.1)$$

where \mathbf{K}_i is the Jacobian of the forward model with respect to the solution state vector at iteration step i . It is numerically calculated using finite differences for \mathbf{x}_{ATM} and by applying the chain rule to Eq. (11) for $[x_{\lambda 1}, \dots, x_{\lambda m}]$. Since the additional surface parameters $[x_{\text{SURF}1}, \dots, x_{\text{SURF}n}]$ are not part of our forward model, their partial derivatives are not included in \mathbf{K}_i .

Each optimization algorithm requires a test for convergence. We use the criterion for the m-form presented in Rodgers (2000):

$$(\mathbf{f}(\mathbf{x}_{i+1}) - \mathbf{f}(\mathbf{x}_i))^T \mathbf{S}_{\delta \mathbf{y}}^{-1} (\mathbf{f}(\mathbf{x}_{i+1}) - \mathbf{f}(\mathbf{x}_i)) < \varepsilon_x m, \quad (A.2)$$

where $\mathbf{S}_{\delta \mathbf{y}}$ is the covariance matrix of the difference between the fit and the measurement; ε_x is a threshold in fraction of variance (here: $\varepsilon_x = 0.01$); and m is the dimension of the measurement vector.

References

- Aoki, T., Hachikubo, A., Hori, M., 2003. Effects of snow physical parameters on shortwave broadband albedos. *J. Geophys. Res.* 108 <https://doi.org/10.1029/2003JD003506>.
- Aoki, T., Hori, M., Motoyoshi, H., Tanikawa, T., Hachikubo, A., Sugiura, K., Yasunari, T., J., Storvold, R., Eide, H.A., Stamnes, K., Li, W., Nieke, J., Nakajima, Y., Takahashi, F., 2007. ADEOS-II/GLI snow/ice products—part ii: validation results using GLI and MODIS data. *Remote Sens. Environ.* 111, 274–290. <https://doi.org/10.1016/j.rse.2007.02.035>.
- Arnaud, L., Picard, G., Champollion, N., Domine, F., Gallet, J.C., Lefebvre, E., Fily, M., Barnola, J., 2011. Measurement of vertical profiles of snow specific surface area with a 1 cm resolution using infrared reflectance: instrument description and validation. *J. Glaciol.* 57, 17–29. <https://doi.org/10.3189/002214311795306664>.
- Bamber, J., Westway, R.M., Marzeion, B., Wouters, B., 2018. The land ice contribution to sea level during the satellite era. *Environ. Res. Lett.* 13 <https://doi.org/10.1088/1748-9326/aac2f0>.
- Berk, A., Bernstein, L.S., Robertson, D.C., 1989. MODTRAN: a moderate resolution model for LOWTRAN7. In: Technical Report GL-TR-89-0122. Air Force Geophysics Laboratory, Hanscom Air Force Base, MA, USA.
- Bohn, N., Guanter, L., Kuester, T., Preusker, R., Segl, K., 2020. Coupled retrieval of the three phases of water from spaceborne imaging spectroscopy measurements. *Remote Sens. Environ.* 242. <https://doi.org/10.1016/j.rse.2020.111708>.

- Brandt, R.E., Warren, S.G., Clarke, A.D., 2011. A controlled snowmaking experiment testing the relation between black carbon content and reduction of snow albedo. *J. Geophys. Res.* 116 <https://doi.org/10.1029/2010JD015330>.
- Carlsen, T., Birnbaum, G., Ehrlich, A., Freitag, J., Heygster, G., Istomina, L., Kipfstuhl, S., Orsi, A., Schäfer, M., Wendisch, M., 2017. Comparison of different methods to retrieve optical-equivalent snow grain size in Central Antarctica. *Cryosphere* 11, 2727–2741. <https://doi.org/10.5194/tc-11-2727-2017>.
- Chandrasekhar, S., 1960. Radiative Transfer. Dover Publications Inc., Mineola, N.Y., USA.
- Clarke, A.D., Noone, K.J., 1985. Soot in the arctic snowpack: a cause for perturbations in radiative transfer. *Atmos. Environ.* 19, 2045–2053. [https://doi.org/10.1016/0004-6981\(85\)90113-1](https://doi.org/10.1016/0004-6981(85)90113-1).
- Colbeck, S.C., 1979. Grain clusters in wet snow. *J. Colloid Interface Sci.* 72, 371–384. [https://doi.org/10.1016/0021-9797\(79\)90340-0](https://doi.org/10.1016/0021-9797(79)90340-0).
- Cook, J.M., Hodson, A.J., Gardner, A.S., Flanner, M., Tedstone, A.J., Williamson, C., Irvine-Flynn, T.D.L., Nilsson, J., Bryant, R., Tranter, M., 2017a. a. Quantifying bioalbedo: a new physically based model and discussion of empirical methods for characterising biological influence on ice and snow albedo. *Cryosphere* 11, 2611–2632. <https://doi.org/10.5194/tc-11-2611-2017>.
- Cook, J.M., Hodson, A.J., Taggart, A.J., Mernild, S.H., Tranter, M., 2017b. b. A predictive model for the spectral “bioalbedo” of snow. *J. Geophys. Res. Earth Surf.* 122, 434–454. <https://doi.org/10.1002/2016JF003932>.
- Cook, J.M., Tedstone, A.J., Williamson, C., McCutcheon, J., Hodson, A.J., Dayal, A., Skiles, M., Hofer, S., Bryant, R., McAree, O., McGonigle, A., Ryan, J., Anesio, A.M., Irvine-Flynn, T.D.L., Hubbard, A., Hanna, E., Flanner, M., Mayanna, S., Benning, L.G., van As, D., Yallop, M., McQuaid, J.B., Grinbin, T., Tranter, M., 2020. Glacier algae accelerate melt rates on the South-Western Greenland ice sheet. *Cryosphere* 14, 309–330. <https://doi.org/10.5194/tc-14-309-2020>.
- Cressie, N., 2018. Mission co2ntrol: a statistical scientist's role in remote sensing of atmospheric carbon dioxide. *J. Am. Stat. Assoc.* 113, 152–181. <https://doi.org/10.1080/01621459.2017.1419136>.
- Dang, C., Fu, Q., Warren, S.G., 2016. Effect of snow grain shape on snow albedo. *J. Atmos. Sci.* 73, 3573–3583. <https://doi.org/10.1175/JAS-D-15-0276.1>.
- Dial, R.J., Ganey, G.Q., Skiles, S.M., 2018. What color should glacier algae be? *FEMS Microbiol. Ecol.* 53.
- Dozier, J., Schneider Jr., S.R., David, F.M., 1981. Effect of grain size and snowpack water equivalence on visible and near-infrared satellite observations of snow. *Water Resour. Res.* 17, 1213–1221.
- Dozier, J., Green, R.O., Nolin, A.W., Painter, T.H., 2009. Interpretation of snow properties from imaging spectrometry. *Remote Sens. Environ.* 113, S25–S37. <https://doi.org/10.1016/j.rse.2007.07.029>.
- Dumont, M., Brissaud, O., Picard, G., Schmitt, B., Gallet, J.C., Arnaud, Y., 2010. High-accuracy measurements of snow bidirectional reflectance distribution function at visible and nir wavelengths – comparison with modelling results. *Atmos. Chem. Phys.* 10, 2507–2520. <https://doi.org/10.5194/acp-10-2507-2010>.
- Flanner, M.G., Zender, C.S., 2006. Linking snowpack microphysics and albedo evolution. *J. Geophys. Res.* 111 <https://doi.org/10.1029/2005JD006834>.
- Flanner, M.G., Zender, C.S., Randerson, J.T., Rasch, P.J., 2007. Present-day climate forcing and response from black carbon in snow. *J. Geophys. Res.* 112 <https://doi.org/10.1029/2006JD008003>.
- Flanner, M.G., Zender, C.S., Hess, P.G., Mahowald, N.M., Painter, T.H., Ramanathan, V., Rasch, P.J., 2009. Springtime warming and reduced snow cover from carbonaceous particles. *Atmos. Chem. Phys.* 9, 2481–2497. <https://doi.org/10.5194/acp-9-2481-2009>.
- Funk, C.C., Theiler, J., Roberts, D.A., Borel, C.C., 2001. Clustering to improve matched filter detection of weak gas plumes in hyperspectral thermal imagery. *IEEE T. Geosci. Remote.* 39, 1410–1420.
- Gallet, J.C., Domine, F., Dumont, M., 2014. Measuring the specific surface area of wet snow using 1310 nm reflectance. *Cryosphere* 8, 1139–1148. <https://doi.org/10.5194/tc-8-1139-2014>.
- Goetz, A.F.H., Vane, G., Salomon, J.E., Rock, B.N., 1985. Imaging spectroscopy for earth remote sensing. *Science* 228, 1147–1153.
- Govaerts, Y.M., Wagner, S., Lattanzio, A., Watts, P., 2010. Joint retrieval of surface reflectance and aerosol optical depth from MSG/SEVIRI observations with an optimal estimation approach: 1. theory. *J. Geophys. Res.* 115, D02203. <https://doi.org/10.1029/2009JD011779>.
- Gray, A., Krolkowski, M., Fretwell, P., Convey, P., Peck, L.S., Mendelova, M., Smith, A.G., Davey, M.P., 2020. Remote sensing reveals antarctic green snow algae as important terrestrial carbon sink. *Nat. Commun.* 11 <https://doi.org/10.1038/s41467-020-16018-w>.
- Green, R.O., Dozier, J., Roberts, D.A., Painter, T.H., 2002. Spectral snow-reflectance models for grain-size and liquid-water fraction in melting snow for the solar-reflected spectrum. *Ann. Glaciol.* 34, 71–73.
- Green, R.O., Painter, T.H., Roberts, D.A., Dozier, J., 2006. Measuring the expressed abundance of the three phases of water with an imaging spectrometer over melting snow. *Water Resour. Res.* 42.
- Green, R.O., Mahowald, N.M., Clark, R.N., Ehlmann, B.L., Ginoux, P.A., Kalashnikova, O.V., Miller, R.L., Okin, G., Painter, T.H., García-Pando, C.P., Realmuto, V.J., Swayze, G.A., Thompson, D.R., Middleton, E., Guanter, L., Dor, E.B., Phillips, B.R., 2018. Nasa's earth surface mineral dust source investigation. *AGU Fall Meet. Abstr.* 24.
- Grenfell, T.C., Warren, S.G., 1999. Representation of a nonspherical ice particle by a collection of independent spheres for scattering and absorption of radiation. *J. Geophys. Res. Atmos.* 104, 31679–31709. <https://doi.org/10.1029/1999JD900496>.
- Guanter, L., Gomez-Chova, L., Moreno, J., 2008. Coupled retrieval of aerosol optical thickness, columnar water vapor and surface reflectance maps from ENVISAT/MERIS data over land. *Remote Sens. Environ.* 112, 2898–2913.
- Guanter, L., Richter, R., Kaufmann, H., 2009. On the application of the MODTRAN4 atmospheric radiative transfer code to optical remote sensing. *Int. J. Remote Sens.* 30, 1407–1424.
- Guanter, L., Kaufmann, H., Segl, K., Foerster, S., Rogass, C., Chabirillat, S., Kuester, T., Hollstein, A., Rossner, G., Chlebek, C., Straif, C., Fischer, S., Schrader, S., Storch, T., Heiden, U., Mueller, A., Bachmann, M., Muehle, H., Mueller, R., Habermeyer, M., Ohndorf, A., Hill, J., Buddenbaum, H., Hostert, P., van der Linden, S., Leitao, P.J., Rabe, A., Doerffer, R., Krasemann, H., Xi, H., Mause, W., Hank, T., Locherer, M., Rast, M., Staenz, K., Sang, B., 2015. The EnMAP spaceborne imaging spectroscopy mission for earth observation. *Remote Sens.* 7, 8830–8857. <https://doi.org/10.3390/rs7070830>.
- Hadley, O., Kirchstetter, W., 2012. Black-carbon reduction of snow albedo. *Nat. Clim. Chang.* 2, 437–440.
- Hamlin, L., Green, R., Mouroulis, P., Eastwood, M., Wilson, D., Dudik, M., Paine, C., 2011. Imaging Spectrometer Science Measurements for Terrestrial Ecology: Aviris and New Developments. *IEEE Aerospace Conference, Big Sky, MT USA*, pp. 1–7.
- Kokhanovsky, A.A., Zege, E.P., 2004. Scattering optics of snow. *Appl. Opt.* 43, 1589–1602. <https://doi.org/10.1364/AO.43.001589>.
- Libois, Q., Picard, G., France, J.L., Arnaud, L., Dumont, M., Carmagnola, C.M., King, M.D., 2013. Influence of grain shape on light penetration in snow. *Cryosphere* 7, 1803–1818. <https://doi.org/10.5194/tc-7-1803-2013>.
- Loizzo, R., Guarini, R., Longo, F., Scopa, T., Formaro, R., Facchinetti, C., Varacalli, G., 2018. PRISMA: The Italian Hyperspectral Mission. *Proc. IGARSS*.
- Malinka, A.V., 2014. Light scattering in porous materials: geometrical optics and stereological approach. *J. Quant. Spectrosc. Radiat.* 141, 14–23. <https://doi.org/10.1016/j.jqsrt.2014.02.022>.
- Mueller, R., Avbelj, J., Carmona, E., Eckhardt, A., Gerasch, B., Graham, L., Guenther, B., Heiden, U., Ickers, J., Kerr, G., Knott, U., Krutz, D., Krawczyk, H., Makarau, A., Miller, R., Perkins, R., Walter, I., 2016. The new hyperspectral sensor DESIS on the multi-payload platform MUSES installed on the ISS. *Int. Arch. Photogramm.* 41, 461–467. <https://doi.org/10.5194/isprsarchives-XLI-B1-461-2016>.
- National Academies of Sciences, Engineering, and Medicine, 2018. Thriving on Our Changing Planet: A Decadal Strategy for Earth Observation from Space. National Academies Press, Washington, DC. <https://doi.org/10.17226/24938>.
- Nolin, A.W., Dozier, J., 1993. Estimating snow grain size using aviris data. *Remote Sens. Environ.* 44, 231–238.
- Nolin, A.W., Dozier, J., 2000. A hyperspectral method for remotely sensing the grain size of snow. *Remote Sens. Environ.* 74, 207–216. [https://doi.org/10.1016/S0034-4257\(00\)00111-5](https://doi.org/10.1016/S0034-4257(00)00111-5).
- Painter, T.H., Dozier, J., 2004a. The effect of anisotropic reflectance on imaging spectroscopy of snow properties. *Remote Sens. Environ.* 89, 409–422. <https://doi.org/10.1016/j.rse.2003.09.007>.
- Painter, T.H., Dozier, J., 2004b. Measurements of the hemispherical-directional reflectance of snow at fine spectral and angular resolution. *J. Geophys. Res.* 109 <https://doi.org/10.1029/2003JD004458>.
- Painter, T.H., Duval, B., Thimas, W.H., 2001. Detection and quantification of snow algae with an airborne imaging spectrometer. *Appl. Environ. Microbiol.* 67, 5267–5272. <https://doi.org/10.1128/AEM.67.11.5267-5272.2001>.
- Painter, T.H., Dozier, J., Roberts, D.A., Davis, R.E., Green, R.O., 2003. Retrieval of subpixel snow-covered area and grain size from imaging spectrometer data. *Remote Sens. Environ.* 85, 64–77. [https://doi.org/10.1016/S0034-4257\(02\)00187-6](https://doi.org/10.1016/S0034-4257(02)00187-6).
- Painter, T.H., Molotch, N., Cassidy, M., Flanner, M., Steffen, K., 2007. Contact spectroscopy for the determination of stratigraphy of snow grain size. *J. Glaciol.* 53, 121–127.
- Painter, T.H., Skiles, S.M., Deems, J.S., Bryant, A.C., Landry, C.C., 2012. Dust radiative forcing in snow of the upper Colorado river basin: 1. a 6 year record of energy balance, radiation, and dust concentrations. *Water Resour. Res.* 48.
- Painter, T.H., Seidel, F.C., Bryant, A.C., Skiles, S.M., Rittger, K., 2013. Imaging spectroscopy of albedo and radiative forcing by light-absorbing impurities in mountain snow. *J. Geophys. Res. Atmos.* 118, 1–13. <https://doi.org/10.1002/jgrd.50520>.
- Painter, T.H., Berisford, D.F., Boardman, J.W., Bormann, K.J., Deems, J.S., Gehrke, F., Hedrick, A., Joyce, M., Laidlaw, R., Marks, D., Mattmann, C., McGurk, B., Ramirez, P., Richardson, M., Skiles, S.M., Seidel, F.C., Winstral, A., 2016. The airborne snow observatory: fusion of scanning lidar, imaging spectrometer, and physically-based modeling for mapping snow water equivalent and snow albedo. *Remote Sens. Environ.* 184, 139–152. <https://doi.org/10.1016/j.rse.2016.06.018>.
- Proksch, M., Löwe, H., Schneebeli, M., 2015. Density, specific surface area, and correlation length of snow measured by high-resolution penetrometry. *J. Geophys. Res. Earth* 120, 346–362. <https://doi.org/10.1002/2014JF003266>.
- Rast, M., Ananasso, C., Bach, H., Dor, E.B., Chabirillat, S., Colombo, R., Bello, U.D., Feret, J.B., Giardino, C., Green, R.O., Guanter, L., Marsh, S., Nieke, J., Ong, C., Rum, G., Schaepman, M., Schlerf, M., Skidmore, A.K., Strobl, P., 2019. Copernicus Hyperspectral Imaging Mission for the Environment – Mission Requirements Document. Technical Report ESA-EOPSM-CHIM-MRD-3216. European Space Agency (ESA), Keplerlaan 1, 2201 AZ Noordwijk, The Netherlands.
- Rodgers, C.D., 2000. Inverse Methods for Atmospheric Sounding: Theory and Practice. World Scientific Pub Co., Oxford, UK.
- Rothman, L.S., Gordon, I.E., Barbe, A., Brenner, D.C., Bernath, P.F., Birk, M., Boudon, V., Brown, L.R., Campargue, A., Champion, J.P., Chance, K., Coudert, L.H., Diana, V., Devi, V.M., Fally, S., Flaud, J.M., Gamache, R.R., Goldman, A., Jacquemart, D.,

- Kleiner, I., Lacome, N., Lafferty, W.J., Mandin, J.Y., Massie, S.T., Mikhailenko, S.N., Miller, C.E., Moazzzen-Ahmadi, N., Naumenko, O.V., Nikitin, A.V., Orphal, J., Perevalov, V.I., Perrin, A., Predoi-Cross, A., Rinsland, C.P., Rotger, M., Simeckova, M., Smith, M.A.H., Sung, K., Tashkun, S.A., Tennyson, J., Toth, R.A., Vandaele, A.C., Auwera, J.V., 2009. The HITRAN 2008 molecular spectroscopic database. *J. Quant. Spectrosc. Radiat.* 110, 533–572. <https://doi.org/10.1016/j.jqsrt.2009.02.013>.
- Schaepman, M.E., Ustin, S.L., Plaza, A.J., Painter, T.H., Verrelst, J., Liang, S., 2009. Earth system science related imaging spectroscopy - an assessment. *Remote Sens. Environ.* 113, S123–S137. <https://doi.org/10.1016/j.rse.2009.03.001>.
- Schaepman-Strub, G., Schaepman, M.E., Painter, T.H., Dangel, S., Martonchik, J.V., 2006. Reflectance quantities in optical remote sensing-definitions and case studies. *Remote Sens. Environ.* 103, 27–42.
- Segl, K., Kuester, T., Rogass, C., Kaufmann, H., Sang, B., Hofer, S., 2012. EeteS - the EnMAP end-to-end simulation tool. *IEEE J. Sel. Top. Appl. Sci.* 5, 522–530. <https://doi.org/10.1109/JSTARS.2012.218894>.
- Seidel, F.C., Ritter, K., Skiles, S.M., Molotch, N.P., Painter, T.H., 2016. Case study of spatial and temporal variability of snow cover, grain size, albedo and radiative forcing in the sierra Nevada and rocky mountain snowpack derived from imaging spectroscopy. *Cryosphere* 10, 1229–1244. <https://doi.org/10.5194/tc-10-1229-2016>.
- Sirguey, P., Mathieu, R., Arnaud, Y., 2009. Subpixel monitoring of the seasonal snow cover with MODIS at 250 m spatial resolution in the southern alps of New Zealand: methodology and accuracy assessment. *Remote Sens. Environ.* 113, 160–181. <https://doi.org/10.1016/j.rse.2008.09.008>.
- Skiles, S.M., Painter, T.H., 2018. Assessment of radiative forcing by light absorbing particles in snow from in situ observations with radiative transfer modeling. *J. Hydrometeorol.* <https://doi.org/10.1175/JHM-D-18-0072.1>.
- Skiles, S.M., Painter, T.H., Okin, G.S., 2017. A method to retrieve the spectral complex refractive index and single scattering optical properties of dust deposited in mountain snow. *J. Glaciol.* 63, 133–147. <https://doi.org/10.1017/jog.2016.126>.
- Stamnes, K., Tsay, S.C., Wiscombe, W., Jayaweera, K., 1988. A numerically stable algorithm for discrete ordinates method radiative transfer in multiple scattering and emitting layered media. *Appl. Opt.* 27, 2502–2509.
- Stibal, M., Box, J.E., Cameron, K.A., Langen, P.L., Yallop, M., Mottram, R.H., Khan, A.L., Molotch, N.P., Chrisman, N.A.M., Quaglia, F.C., Remias, D., Smeets, C.J.P., van den Broecke, M.R., Ryan, J.C., Hubbard, A., Tranter, M., van As, D., Ahlström, A.P., 2017. Algae drive enhanced darkening of bare ice on the Greenland ice sheet. *Geophys. Res. Lett.* 44, 11463–11471.
- Takeuchi, N., Dial, R., Kohshima, S., Segawa, T., Uetake, J., 2006. Spatial distribution and abundance of red snow algae on the harding icefield, alaska derived from a satellite image. *Geophys. Res. Lett.* 33 <https://doi.org/10.1029/2006GL027819>.
- Thompson, D.R., Gao, B.C., Green, R.O., Roberts, D.A., Dennison, P.E., Lundeen, S.R., 2015. Atmospheric correction for global mapping spectroscopy: Atrem advances for the hyperspectral preparatory campaign. *Remote Sens. Environ.* 167, 64–77. <https://doi.org/10.1016/j.rse.2015.02.010>.
- Thompson, D.R., Natraj, V., Green, R.O., Helmlinger, M.C., Gao, B.C., Eastwood, M.L., 2018. Optimal estimation for imaging spectrometer atmospheric correction. *Remote Sens. Environ.* 216, 355–373. <https://doi.org/10.1016/j.rse.2018.07.003>.
- Toon, O.B., McKay, C.P., Ackerman, T.P., Santhanam, K., 1989. Rapid calculation of radiative heating rates and photodissociation rates in inhomogeneous multiple scattering atmospheres. *J. Geophys. Res.* 94, 287–301.
- Tuzet, F., Dumont, M., Arnaud, L., Voisin, D., Lamare, M., Larue, F., Revuelto, J., Picard, G., 2019. Influence of light-absorbing particles on snow spectral irradiance profiles. *Cryosphere* 13, 2169–2187. <https://doi.org/10.5194/tc-13-2169-2019>.
- Tuzet, F., Dumont, M., Picard, G., Lamare, M., Voisin, D., Nabat, P., Lafayesse, M., Larue, F., Revuelto, J., Arnaud, L., 2020. Quantification of the radiative impact of light-absorbing particles during two contrasted snow seasons at col du lautaret (2058 m a.s.l., french alps). *Cryosphere* 14, 4553–4579. <https://doi.org/10.5194/tc-14-4553-2020>.
- van Diedenhoven, B., Ackerman, A.S., Cairns, B., Fridlind, A.M., 2014. A flexible parameterization for shortwave optical properties of ice crystals. *J. Atmos. Sci.* 71, 1763–1782. <https://doi.org/10.1175/JAS-D-13-0205.1>.
- Warren, S.G., 1982. Optical properties of snow. *Rev. Geophys.* 20, 67–89. <https://doi.org/10.1029/RG020i001p00067>.
- Warren, S.G., 2019. Optical properties of snow and ice. *Phil. Trans. R. Soc. A* 337. <https://doi.org/10.1098/rsta.2018.0161>.
- Warren, S.G., Wiscombe, W.J., 1980. A model for the spectral albedo of snow. II: snow containing atmospheric aerosols. *J. Atmos. Sci.* 37, 2734–2745. [https://doi.org/10.1175/1520-0469\(1980\)037<2734:AMFTSA>2.0.CO;2](https://doi.org/10.1175/1520-0469(1980)037<2734:AMFTSA>2.0.CO;2).
- Williamson, C.J., Anesio, A.M., Cook, J., Tedstone, A., Poniecka, E., Holland, A., Fagan, D., Tranter, M., Yallop, M.L., 2018. Ice algal bloom development on the surface of the Greenland ice sheet. *FEMS Microbiol. Ecol.* 94.
- Wiscombe, W.J., 1980. Improved Mie scattering algorithms. *Appl. Opt.* 19, 1505–1509.
- Wiscombe, W.J., Warren, S.G., 1980. A model for the spectral albedo of snow. I: pure snow. *J. Atmos. Sci.* 37, 2712–2733. [https://doi.org/10.1175/1520-0469\(1980\)037<2712:AMFTSA>2.0.CO;2](https://doi.org/10.1175/1520-0469(1980)037<2712:AMFTSA>2.0.CO;2).
- Yallop, M.L., Anesio, A.M., Perkins, R.G., Cook, J., Telling, J., Fagan, D., MacFarlane, J., Stibal, M., Barker, G., Bellas, C., Hodson, A., Tranter, M., Wadham, J., Roberts, N.W., 2012. Photophysiology and albedo-changing potential of the ice algal community on the surface of the Greenland ice sheet. *ISME J.* 6, 2302–2313. <https://doi.org/10.1038/ismej.2012.107>.
- Zege, E., Katsev, I., Malinka, A., Prikhach, A., Polonsky, I., 2008. New algorithm to retrieve the effective snow grain size and pollution amount from satellite data. *Ann. Glaciol.* 49, 139–144. <https://doi.org/10.3189/172756408787815004>.
- Zege, E.P., Katsev, I.L., Malinka, A.V., Prikhach, A.S., Heygster, G., Wiebe, H., 2011. Algorithm for retrieval of the effective snow grain size and pollution amount from satellite measurements. *Remote Sens. Environ.* 115, 2674–2685. <https://doi.org/10.1016/j.rse.2011.06.001>.